FAILURE MECHANISM OF ROLLING SHEAR FAILURE IN CROSS-LAMINATED TIMBER

by

Xin Nie
B.Sc., The University of British Columbia, 2011

A THESIS SUBMITTED IN PARTIAL FULFILLMENT OF
THE REQUIREMENTS FOR THE DEGREE OF

MASTER OF SCIENCE

in

The Faculty of Graduate and Postdoctoral Studies

(Forestry)

THE UNIVERSITY OF BRITISH COLUMBIA
(Vancouver)

November 2015

© Xin Nie, 2015

Abstract

Wood as building material is gaining more and more attention in the 21st century due to its positive attributes such as light weight, renewability, low carbon footprint and fast construction period. Cross-laminated timber (CLT), as one of the new engineered wood products, requires more research emphasis since its mechanical performance can allow CLT to be utilized in massive timber structures.

This thesis focuses on revealing one of the key failure mechanisms of CLT, which is usually referred to as the rolling shear failure. The scientific research conducted in this thesis combined both analytical modelling and experimental material testing.

The stresses in CLT cross-layers obtained from a finite-element model were analyzed to differentiate various failure modes possible. Tension perpendicular to grain stress was found to cause cross-layer failure in combined with the rolling shear stress. Experimentally, specimens prepared from 5-layer CLT panels were tested under center-point bending condition. Detailed failure mechanism of CLT cross-layers were recorded with high speed camera to capture the instant when initial failure happened. It is evident that some of the specimens failed in tension perpendicular to grain which verified the modelling results. Variables such as the rate of loading and the manufacturing clamping pressure were designed in experiments to compare their influence to the failure of CLT specimens.

In this research, the failure of CLT cross-layer was updated to a combined consequence of both rolling shear stress and tension perpendicular to grain stress. Future research topics and product improvement potentials were given by the end of this thesis.

Preface

This thesis and its related research are focused on the failure mechanism of rolling shear failure in CLT. Under the supervision and guidance of Dr. Frank Lam, Dr. Ricardo O. Foschi and Dr. Stavros Avramidis, this thesis is the original and unpublished work of the author Xin Nie.

Chapter 3 includes a finite element modelling of a CLT beam. This model was developed and modified based on the model established by Dr. Yuan Li in his thesis to evaluate the duration-of-load and size effects on the rolling shear strength of CLT. The original ANSYS codes from Dr. Yuan Li was modified to suit the objectives of this thesis and its research.

Chapter 4 develops laboratory experiments on CLT specimens. Test specimens were cut and prepared by Mr. George Li and Mr. Chao Zhang from the laboratory of the Centre of Advanced Wood Processing (CAWP). All the experiments were conducted under the supervision of Dr. Frank Lam.

Table of Contents

Abstract ii
Preface iv
Table of Contents v
List of Tables viii
List of Figures ix
Acknowledgements xi
Dedication xii
1. Introduction 1
1.1. Background 1
1.2. Objectives 3
1.3. Methods 5
1.4. Thesis Organization 6
2. Literature Reviews 7
2.1. A Brief Introduction of Engineered Wood Products 7
2.2. Cross-laminated Timber 8
2.3. Rolling Shear Failure of CLT 10
3. Modeling of Failure Mechanism of CLT 12
3.1. Introduction 12
3.2. Materials and Methods 13
3.2.1. Software Platform 13
3.2.2. Modelling of CLT Beams 13
3.2.2.1. Model Configurations 14
3.2.2.2. Gaps between Cross-layer Boards 17
3.2.2.3. Modeling of Glue and Clamping Pressure 18
3.2.2.4. Coordination System and Wood Grains 19
3.2.2.5. Determining the Load 19
3.2.3. Analysis Methods 20
3.2.3.1. Nodal Selection and Stress Information Extraction 20

3.2.3.2. Mohr’s Circle Analysis 22
3.3. Results and Discussion 25
3.3.1. CLT Model Presentation 25
3.3.2. Nodal Selection and Stress Results 27
3.3.3. Mohr’s Circle Analysis 28
3.3.4. Tension Failure and Rolling Shear Failure 33
3.3.5. Conclusions 36
4. Mechanical Testing of CLT Specimens 37
4.1. Introduction 37
4.2. Materials and Methods 38
4.2.1. Materials 38
4.2.2. Materials Preparation 40
4.2.3. Testing Set-up 43
4.2.3.1. Testing Standards 43
4.2.3.2. Testing Machine 43
4.2.3.3. Modulus of Elasticity (MOE) Tests and Deflectometer 43
4.2.3.4. Ultimate Load Tests 44
4.2.3.5. Failure Criteria 44
4.2.3.6. Loading Rate 45
4.2.3.7. High Speed Camera Video Capture 45
4.2.4. Methods 49
4.2.4.1. Calculating the Modulus of Elasticity 49
4.2.4.2. Specimens Re-categorization 52
4.2.4.3. Failure Mode Analysis 53
4.2.4.4. Initial Failure Modes and Annual Ring Orientations 53
4.3. Results and Discussion 53
4.3.1. Modulus of Elasticity of Specimens 53
4.3.2. Re-categorizing the Specimens of 0.1MPa CLT 59
4.3.3. Testing Specimens under Different Loading Rates 60
4.3.4. Initial Failure Modes of CLT Specimens 63

4.3.5. Faster Loading Rate and Initial Failures 76
4.3.6. Initial Failure Modes and Annual Ring Orientations 81
4.4. Conclusions.. 87
5. Conclusions and Recommendations 89
5.1. General Conclusions 89
5.2. Recommendations for Further Research 91
Bibliography 93
Appendix 96
Appendix A. Dimensions for all testing specimens with 0.1 MPa manufacturing clamping pressure 96
Appendix B. Dimensions for all testing specimens with 0.4 MPa manufacturing clamping pressure 100
Appendix C. Modulus of Elasticity of 93 specimens from 0.1 MPa manufacturing clamping pressure panels 103
Appendix D. Modulus of Elasticity of 60 specimens from 0.4 MPa manufacturing clamping pressure panels 105
Appendix E. Ultimate loads for slower loading rate specimens 106
Appendix F. Ultimate loads for faster loading rate specimens 107
Appendix G. Ultimate loads for 60 specimens with manufacturing clamping pressure of 0.4 MPa 108
Appendix H. The initial failure modes of 65 specimens successfully captured with high speed camera filming 109

List of Tables

Table 3-1 Dimensions of the Hem-Fir 5-layer CLT model 16
Table 3-2 Mechanical properties of two grades of lumber used in the model 17
Table 3-3 Bonding stiffness of the glue lines for different clamping pressures 19
Table 3-4 Nodes selected and their coordinate information 27
Table 3-5 Stress information for selected nodes 28
Table 3-6 Average normal stress and radii for six selected nodes 28
Table 4-1 Specimens dimensions weights, and moisture contents 41
Table 4-2 0.1 MPa 93 specimens MOE statistics 54
Table 4-3 0.4 MPa 60 specimens MOE statistics 56
Table 4-4 0.4 MPa 60 specimens MOE statistics 58
Table 4-5 Test statistics of S, M, and L groups of 0.1 MPa specimens 59
Table 4-6 Test statistics of specimens under various loading rates 60
Table 4-7 Failure modes statistics for specimens.. 72
Table 4-8 Comparisons of the test statistics of three different loading rates 80
Table 4-9 Statistics of 65 specimens by their initial failure modes and the crack-to-grain angle type 83

List of Figures

Figure 1-1 Examples of three, five and seven layers CLT panels 3
Figure 2-1 An example of a three layers CLT panel 9
Figure 3-1 5-layer Hem-Fir CLT beam finite element modeling with elements 15
Figure 3-2 Geometrical configurations of 5-layer CLT beam finite element modeling ... 15
Figure 3-3 Gaps between cross-layer boards 18
Figure 3-4 Information from six nodes extracted for analysis 21
Figure 3-5 Original stresses and stresses at an incline plane. 22
Figure 3-6 A sample of Mohr's circle 24
Figure 3-7 ANSYS model of CLT 5-Layer Hem-Fir specimen 26
Figure 3-8 Mohr's circle of selected node No.3 29
Figure 3-9 Six selected nodes and their Mohr's circles. 34
Figure 4-1 Grades of panels used to manufacture the CLT panels 40
Figure 4-2 Reference lines system used in the testing. 42
Figure 4-3 High speed camera set up 47
Figure 4-4 General test set-up.. 48
Figure 4-5 The stress-strain relationship for wood products 50
Figure 4-6 Cumulative distribution curve of the MOEs of 0.1MPa CLT specimens.. 54
Figure 4-7 Cumulative distribution curve of the MOEs of 0.4MPa CLT specimens. 56
Figure 4-8 Cumulative MOEs of both 0.1 MPa and 0.4 MPa CLT specimens.. 57
Figure 4-9 Three images of the specimen under center-point load. 65
Figure 4-10 Reference line system 67
Figure 4-11 The initial failure instant of specimen HF0.4-(3)-23. 69
Figure 4-12 An example of rolling shear type of failures 71
Figure 4-13 Specimen HF0.4-(3)-25, a marginal initial failure. 75
Figure 4-14 The initial failure instant of specimen HF0.4-(3)-28 77

Figure 4-15 The initial failure instant of specimen HF0.4-(3)-30 79
Figure 4-16 Three types of failure cracks 82
Figure 4-17 An example of Type A failure from specimen HF-0.4MPa-(3)-12 83
Figure 4-18 An example of Type B failure from specimen HF-0.4MPa-(3)-43. 85
Figure 4-19 An example of Type C failure from specimen HF-0.4MPa-(3)-36 86

Acknowledgements

With this opportunity, I would like to offer my enduring gratitude to all faculty members, staff and my fellow students at the UBC, who have provided generous help and support to my research and work. I owe particular thanks to Dr. Frank Lam, my Master's supervisor, who has patiently inspired me to continue my work and fatherly taken care of all our fellow students in the past two years.

Special gratitude goes to Dr. Ricardo O. Foschi and Dr. Stavros Avramidis, who have been my Master's committee members and provided me with great guidance and encouragement to my research and study.

Appreciation is also given to Mr. George Li and Mr. Chao Zhang who provided selfless help with the preparation of specimens and testing machine set-up from the CAWP laboratory.

I am also very grateful to NSERC (Natural Sciences and Engineering Research Council of Canada) strategic research Network for Engineered Wood-based Building Systems for its support in this research.

Finally, affections and gratitude go to my parents and wife who have supported my education at UBC, both morally and financially. I also thank my forthcoming child that you have greatly encouraged me during the last phase of my Master's study.

To my parents, my beloved wife, and my first child

1. Introduction

1.1. Background

Known as one of the oldest building materials in human civilization, wood with its unique advantages overmatches others in many aspects. Used for buildings, weapons, tools and furniture as early as the Paleolithic times, wood is regarded of very high aesthetical value while it also has strengths in mechanical performance, thermal properties, sound isolation, and so on.

The first form of wood building was the log home which was completely built out of logs. As the industrial times arrived with tremendous advancement in engineering technology, logs were then debarked and processed into smaller pieces known as timber and dimensional lumber. Lumber provides good material uniformity and structural stability for building construction, as timber buildings are one of the major building types still in use today. However, the popularity of steel and concrete construction seemingly prevailed over timber buildings in the 20th century, as more skyscrapers and towers built with steel and concrete seized more attention.

In the 21st century, with growing global awareness of green buildings and low carbon footprints, timber buildings are once again gaining attentions in both residential and commercial markets. Tackling more and more stringent building codes in North America and Europe, dimensional lumber may no longer sufficiently meet modern designing and constructional demands for larger and taller buildings. In this environment, engineered wood products, especially structural products, have become a group of very important research subjects around the world.

According to an article from the Forest Products Journal (Guss 1995), engineered wood products are defined as any structural products made from smaller wood pieces processed from logs. These smaller pieces of wood are glued together with certain adhesive bonding agent to form final products with specified mechanical properties. Many good examples of engineered wood products have been widely used for a long time, such as Glulam, plywood, OSB (oriented strand board), LVL (laminated veneer lumber), and of course, cross-laminated timber which is usually referred as CLT. Among all these different products, this thesis focuses on CLT and its failure mechanism as the research subjects.

Cross-laminated timber, as a comparatively new member of the engineered wood products family, was first introduced in Austria in the early 1990's (Zhou et al., 2014). Similar to plywood, product of CLT can be defined by its unique design of at least three layers of orthogonally alternating lumber lamina which are glued in between. The most common CLT panels are those of three, five or seven layers. Figure 1.1 shows the cross-sections of these three types of CLT panels. As it shows in the image, layers are orthogonally glued to the neighboring layers.

Figure 1-1 Examples of three, five and seven layers CLT panels. This figure shows the cross-sections of these panels. (Image source: HYBRiD Build Solutions)

1.2. Objectives

When using CLT as a structural material in building constructions, the failure modes are needed to be evaluated to predict failure patterns and propose product improvements. As a naturally grown material, wood is an anisotropic material which means that different mechanical properties are found in different axes of wood. The wood material fails when the stress in any axis exceeds the corresponding strength. In CLT, when loaded out of the plane, cross-layers are subjected to shear stress. The shear strength of the cross layer is a very weak property which governs the capacity of the entire CLT panel or beam. The shear stress in cross-layers is usually referred to as the rolling shear stress, which can be noted from a book in 1989 introducing the mechanical performance evaluation of plywood (Stalnaker & Harris, 1989). This book also mentioned that the rolling shear was first found in plywood layers which were perpendicular to the face layers, or called the cross-band. When plywood was subjected to shear forces, veneer plies that are perpendicularly oriented would be stressed in rolling shear (Biblis, 2000). According to an academic research paper (Mestek et al., 2008), the shear capacity in CLT cross-layers is considerably lower than the shear capacity parallel to grain. The Wood Handbook (FPL, 2010) also mentioned that the rolling shear capacity in solid-sawn wood is only about 18 to 28 percent of the shear strength parallel to the grain direction, according to limited test results.

The weak rolling shear capacity in CLT cross-layers governs the bending performance of CLT, especially under short span bending condition where the beam is subject to high shear loads. However, no test has been taken on to study the failure mechanism of CLT and how rolling shear stress causes initial material failure. This thesis and its related research are aimed to discover the failure mechanism of CLT and to determine if the failure in cross-layers is solely due to the low rolling shear capacity or any other possible reasons. The reveal of the actual failure mechanism of CLT will theoretically support future improvement or reinforcement of CLT products.

1.3. Methods

In this thesis, the research of the failure mechanism of CLT cross-layers was conducted in a fashion that combined both computer finite-element modeling and laboratory testing on CLT specimens. The finite-element model provided stress distributions of a CLT beam under certain level of center-point bending load. With in-depth evaluation of the stress output, possible failure modes were predicted based on the model. In the laboratory testing, CLT specimens of the same size as the finite-element model were prepared from CLT panels. Totally 150 specimens were tested under center-point loading condition. During the testing procedure, variables were designed to compare the differences between various loading rates and panel manufacturing clamping pressures. To record the failure instants of the cross-layers of CLT, a high speed camera was used to monitor each test. More failure modes analysis was done with the images captured by this camera. The initial failure modes of these 150 specimens were then categorized to three groups, namely the tension perpendicular to grain failure, the rolling shear failure and the marginal failure. Based on the initial failure modes analysis, results were then compared with the finite-element model to draw conclusions on the failure mechanism of CLT cross-layers. Last but not the least, the initial failure modes of CLT cross-layers were also compared with the failure crack to annual ring orientations to seek connections in between.

1.4. Thesis Organization

In this thesis, there are five chapters in total. Other than this introduction chapter, the rest of the chapters mainly focus on the following different research aspects.

Chapter 2 gives introduction and discussion of previous literatures on relative topics about CLT, such as the history and development, the manufacturing process, the rolling shear capacity of CLT and also ways to reinforce CLT beams and panels from previous research and study.

Chapter 3 focuses on the finite-element modeling of a CLT beam. This chapter included the modeling procedure and details, as well as the analytical methods and results. Possible failure modes are proposed by the end of this chapter.

Chapter 4 describes the laboratory experiments of 150 CLT specimens. All the testing details are given in this chapter, along with the testing results and methods of analysis. High speed camera images will also be demonstrated and discussed. Some conclusions will be made regarding the failure mechanism of CLT.

Chapter 5 concludes the research objectives and method of this thesis, and gives cross-comparisons and conclusions of the failure mechanism of CLT cross-layers. Possible future research topics and CLT products improvement suggestions are provided by the end of this chapter.

2. Literature Reviews

This section of the thesis includes literature reviews of previous studies on the failure mechanism of CLT which have been referred to as the rolling shear failure. Results and conclusions from previous studies establish the fundamental knowledge groundwork for the research conducted in this thesis. The background of engineered wood products, the history and development of CLT and the related research on the rolling shear failure of CLT will be discussed in this chapter.

2.1. A Brief Introduction of Engineered Wood Products

The concept and crude practice of engineered wood products could be traced back to more than a thousand years ago when ancient Egyptian and Chinese people shaved trees into smaller segments and then glued them together for furniture (Williamson, 2002). Modern engineered wood industry originated in the early 20th Century in North America with plywood products ruling the market for more than 50 years (Williamson, 2002). With tremendous advancement in manufacturing technology in the second half of the last Century, many innovative engineered wood products were invented including laminated veneer lumber (LVL), wood I-joist, glulam beams, oriented-strand board and so on (Guss, 1995).

Given more and more attention in research and practice, new engineered wood products are having shorter wait time between its invention and final application in construction industry (Guss, 1995). Compared to solid-sawn lumber, engineered wood products possess advantages in many aspects. First, possible longer span of engineered wood products provides more design flexibility for architects. The reliability and predictability with known strength properties also make engineered wood products well-used in building constructions. Moreover, engineered wood products utilize small diameter logs which were of little value before. According to a report, the increasing demand of timber and rising price of wood are shifting the market from solid-sawn lumber to engineered wood products (McKeever, 1997). With all these advantages, there is a bright future for engineered wood products.

2.2. Cross-laminated Timber

Cross-laminated timber was invented decades ago, however, in the recent ten years, CLT has become a popular research topic worldwide because of its many advantages. Previous study on CLT noted that it was invented in Switzerland in 1970’s and first used as a building material in Austria, Europe in 1993 (Zhou, 2010). CLT is usually manufactured as panel products of which layers of solid-sawn lumber are glued in an orthogonally alternating fashion. Figure 2-1 demonstrates an example of a three layers CLT panel. This design efficiently reduces the anisotropic property of wood and brings excellent structural stability to CLT products.

Figure 2-1 An example of a three layers CLT panel. (Image source: Nordic X-Lam)

CLT owns unique advantages compared to other building materials such as concrete, steel or even structural timber products as glulam. According to a product report from Structurlam (2013), CLT in building constructions is 6 times lighter and 1/3 space saving compared to concrete structures. With higher grade lumber on the surface layers, CLT owns very high aesthetical values while it doesn’t necessarily require extra finishing work (Structurlam, 2013). The orthogonal boards design reduces shrinkage or swelling, at the same times, allows loads to be transfers in more than one direction (Zhou, 2010).

Globally, many successful CLT buildings have been constructed. Since 1990’s, CLT has been used in multiple-stories timber buildings. The famous nine stories Murray Grove in London is one of the tallest CLT buildings so far of which the elevator shaft was made from CLT as well (Yates et al. 2008). Several seismic tests conducted in Japan on 3 to 7 stories CLT buildings also showed very good earthquake performance (Ceccotti, 2008).

2.3. Rolling Shear Failure of CLT

Despite all the advantages of CLT as a structural material, the weak rolling shear property of CLT cross-layers has become the research concentration for CLT's utilization under heavy load. From Li's report of evaluating CLT's rolling shear strength properties (2014), rolling shear stress was defined as the shear stress in the radial-tangential plane of wood which was perpendicular to the longitudinal grain direction. The rolling shear is not an intrinsic material property but an apparent substitute quantity of a structure, according to Aicher and Dill-Langer (2000). As an anisotropic natural material, the strength and stiffness of shear in radial-tangential plane of wood is significantly lower than those of the longitudinal plane. According to Wood Handbook (FPL, 2010), limited tests data showed that the rolling shear strength in softwood lumber only accounts for 18 to 28 percent of the shear strength parallel to grain. The low rolling shear capacity, under circumstances such as concentrated loads or short-span, is a topic engineers must concern about. In structural design, introducing high rolling shear stress should be avoided if possible.

The rolling shear strengths vary with factors such as the wood species, grade of lumber used to manufacture, the manufacturing clamping pressure, etc. From Yawalata and Lam (2011), the rolling shear strength tested from a 3-layers Spruce-Pine-Fir (SPF) CLT panel was 2.22 MPa from the center-point bending tests. However, another test showed that the rolling shear strength of SPF wooden cross-layer from two-plate shear tests was only 1.09 MPa (Zhou, et al., 2014). Zhou, et al. claimed that the difference between the test results was caused by the grade of laminates and the manufacturing pressure (0.1 MPa and 0.4 MPa). Zhou, et al. concluded that higher manufacturing pressure or better cross-layer lumber quality resulted in higher rolling shear strength. According to a study by Fellmoser and Blaß (2004), the low rolling shear capacity causes significant shear deformation in the cross-layers of CLT.

The low rolling shear capacity of wood has restricted the uses of products such as CLT panels. Since the rolling shear strength varies and is hard to specify for each single product, European Eurocode 5 has uniformly characterized the rolling shear strength of wood as 1.0 MPa despite the wood strength class (2004). In Canada, the absence of code regulations of the low rolling shear capacity has made it challenging to design and use products such as CLT. The code establishment and more research concentration on CLT rolling shear are necessary to extensively promote innovative engineered structural timber products into the industry.

3. Modeling of Failure Mechanism of CLT

3.1. Introduction

CLT is an engineered wood product with unique failure mechanism due to the arrangement of orthogonally glued wooden boards. In bending conditions, mechanical properties of the cross-layers of CLT can govern the capacity of the entire beam under high depth to span ratio or with high shear forces from point support. In these cases the relatively weak rolling shear strength in cross-layers of CLT is believed to be the governing property of the material. According to Wood Handbook, tests showed that for solid-sawn timber, the average rolling shear strengths only account for 18 to 28 percent of the shear strengths parallel to grain direction (FPL, 2010). However, no research so far has considered the influence of tension or compression stresses perpendicular to grain in the cross-layers resulting from the internal shear forces of the member under bending. Both of these material properties can be as low as about only 10 percent of the tension or compression strengths parallel to the grain direction. The failure mechanism of the cross layer in a CLT member under bending needs to be further studied considering both the normal stresses perpendicular to grain and the rolling shear stress.

To better understand the failure mechanism of CLT, a finite element model was established to study the physical and mechanical behaviors of CLT in a mathematical modelling process. Corresponding to the laboratory tests done in this study, which involved only 5 layers CLT specimens made from Hem-Fir, the modeling of CLT also focuses on a 5 layers CLT beam with similar geometrical and mechanical properties as the tested specimens.

3.2. Materials and Methods

3.2.1. Software Platform

All of the modeling work in this chapter was done with commercial finite-element program ANSYS v14.0 (SAS, 2011).

3.2.2. Modelling of CLT Beams

To analyze the failure of the cross layer in a CLT member under bending condition, a 5-layer Hem-Fir CLT model was made. The modeling was originally prepared by Dr. Y. Li from the University of British Columbia as part of his doctoral dissertation (Li, 2015) to study the rolling shear stresses of CLT member under duration of load effect. The model was used in this study to evaluate the failure mechanism of CLT cross-layers under bending.

The geometrical configurations of this finite element model were similar to the actual tested specimen which will be introduced in this section. In the modeling process of this CLT beam, a Cartesian coordination system with three axes was used. To model the orthotropic property of CLT, SOLID45 element type was used in this model with material properties simulating Hemlock-Fir species group. Moreover, some CLT details were also modeled, such as the gaps between cross-layer boards and the glue properties. However, the complex details associated with stochastic annual ring orientation in the radial-tangential plane of the wood were ignored. Since this model was established based on Cartesian coordination system, however, if polar coordination system were used, the radial and tangential stresses would be different considering the ring orientations of wood. Future research should model the CLT cross-layers with polar coordination system to demonstrate various possible annual ring orientations.

3.2.2.1. Model Configurations

This model was established based on the ANSYS Parametric Design Language (APDL) which allowed high degree of freedom of parameterization of model configurations. After adjusting the original APDL script, the model was modified to similar geometrical configurations as the laboratory tested specimens. Figure 3-1 shows the finite element model with elements of the modified 5-layer CLT model used in this study. Figure 3-2 shows the geometrical configurations of this model as the cross-layer boards were orthogonally arranged to the longitudinal layers.

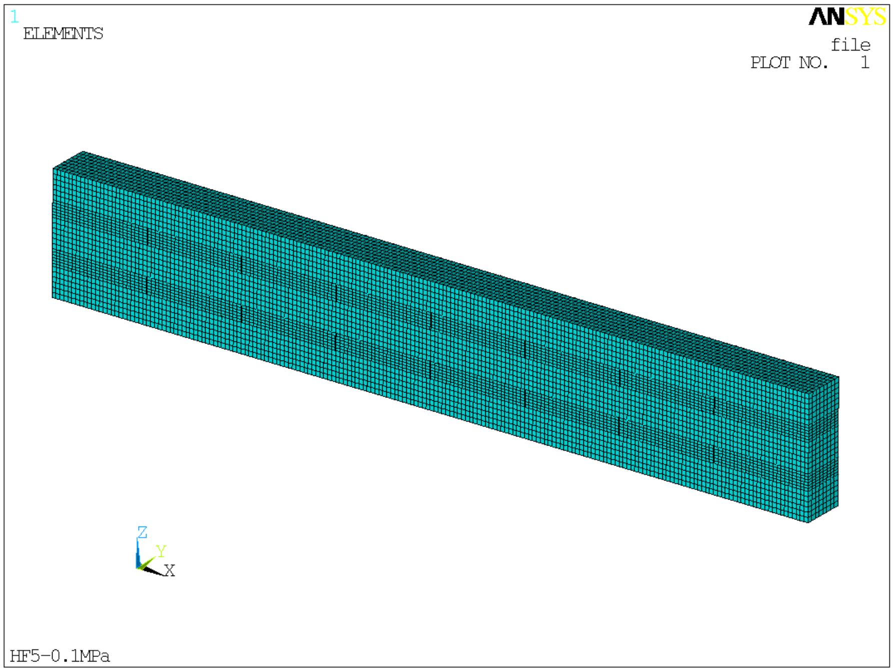

Figure 3-1 5-layer Hem-Fir CLT beam finite element modeling with elements

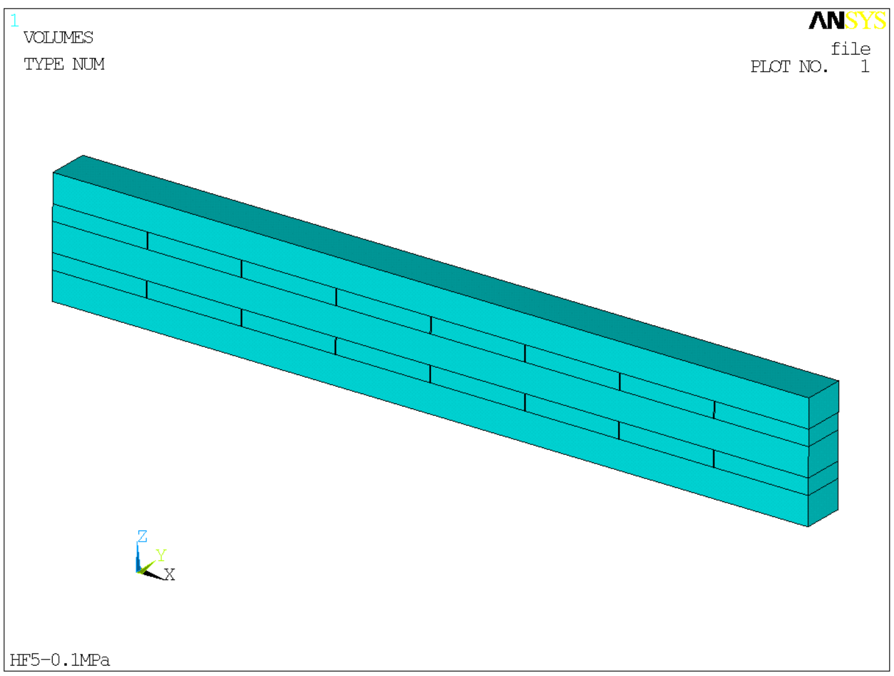

Figure 3-2 Geometrical configurations of 5-layer Hem-Fir CLT beam finite element modeling

The dimensions of this model resemble the actual test specimens which will be introduced in the following chapter. This 5-layer CLT model includes five different layers where the second and fourth layers are cross-layers. As Figure 3-2 shows, each cross-layer contains eight boards in the model, which is also consistent with the real specimen tested. The cross-layers have thickness of 19 mm, which is thinner than the longitudinal layers of which the thickness was 34mm. Table 3-1 gives the dimensions of this 5-layer CLT model.

Table 3-1 Dimensions of the Hem-Fir 5-layer CLT model

<table>
<tr><th colspan="2">Model</th><th>Length (mm)</th><th>Width (mm)</th><th>Thickness (mm)</th></tr>
<tr><td colspan="2">Overall Beam Dimension</td><td>914.4</td><td>50.8</td><td>140.0</td></tr>
<tr><td rowspan="5">Laminate from top to bottom</td><td>Laminate 1</td><td>914.4</td><td>50.8</td><td>34.0</td></tr>
<tr><td>Laminate 2</td><td>914.4</td><td>50.8</td><td>19.0</td></tr>
<tr><td>Laminate 3</td><td>914.4</td><td>50.8</td><td>34.0</td></tr>
<tr><td>Laminate 4</td><td>914.4</td><td>50.8</td><td>19.0</td></tr>
<tr><td>Laminate 5</td><td>914.4</td><td>50.8</td><td>34.0</td></tr>
</table>

As mentioned in Chapter 4, the 5-layer CLT specimen was manufactured with two different grades of lumber. The outmost layers which mean the top and bottom were manufactured with L1 grade hemlock lumber, while three layers in the middle were L2 grade. The original model also included this into the modeling with two sets of orthotropic material defined for various grades of lumber. To keep the consistency with the original model, the material properties used in this model are remained same with the original model. Table 3-2 gives the basic mechanical properties for these two grades of lumber in this model. It is worth to mention that the subscriptions in Table 3-2, the “L”, ”T” and ”R” represent three major fiber directions in wood, which represent longitudinal, tangential and radial directions. The fiber directions in the longitudinal layers and cross layers in CLT are different, as CLT layers are orthogonally alternating.

Table 3-2 Mechanical properties of two grades of lumber used in the model

<table>
<tr><th rowspan="2">Laminate</th><th rowspan="2">Grade</th><th colspan="4">Elastic properties (GPa)</th><th colspan="3">Poisson's Ratio</th></tr>
<tr><th>E_L</th><th>E_T & E_R</th><th>G_{LR} & G_{LT}</th><th>G_{RT}</th><th>ν_{LR}</th><th>ν_{LT}</th><th>ν_{RT}</th></tr>
<tr><td>1,5</td><td>L1</td><td>11.43</td><td>0.381</td><td>0.714</td><td>0.071</td><td rowspan="2">0.316</td><td rowspan="2">0.347</td><td rowspan="2">0.469</td></tr>
<tr><td>2,3,4</td><td>L2</td><td>10.66</td><td>0.355</td><td>0.666</td><td>0.067</td></tr>
</table>

3.2.2.2. Gaps between Cross-layer Boards

When CLT is manufactured, small gaps between boards are usually presented. This CLT model also simulated the gaps into its design. The consideration of the gaps between boards in cross-layers is important, since the shear stress distribution is changed when there is zero rolling shear stress near the gap edges. In this model, the gap remains as about one millimeter as the original model. The impact of this gap can be further studied in the future. Figure 3-3 indicates the gap between boards in the cross-layers in this model.

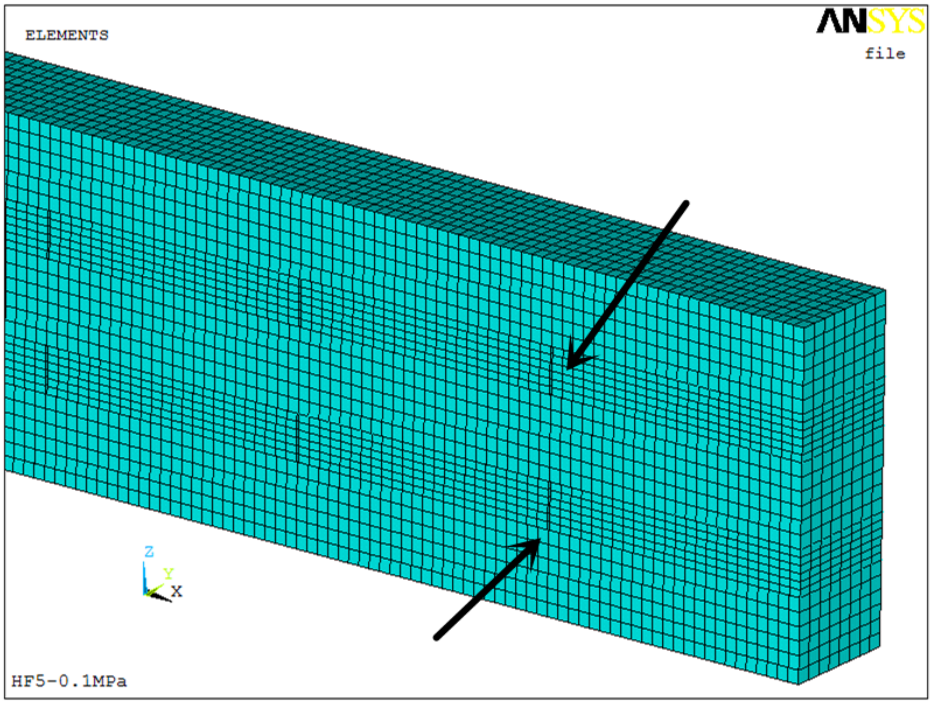

Figure 3-3 Gaps between cross-layer boards. Arrows shows the location of these gaps. The width of these gaps is about 1 mm. Rolling shear stress is zero on the edges of these gaps.

3.2.2.3. Modeling of Glue and Clamping Pressure

During the manufacturing process of CLT, glue was applied between laminates prior to pressing and curing. For the test specimen used in this study, polyurethane was used to manufacture Hem-Fir 5-layer CLT beams. The heat press generates variable pressures when curing the glue in CLT, which is usually referred to as the clamping pressure. To model the mechanical behaviors of the glue lines, COMBIN14 linear x-y-z spring pairs were used in this model to resemble the bonding stiffness between laminates. Based on a test database by Schaaf (2010), glue line shear stiffness at clamping pressures of 0.1

MPa and 0.4 MPa are shown in Table 3-3. In this study, the model used the glue bonding stiffness associated with 0.1 MPa clamping pressure. Moreover, the bonding stiffness is also assumed non-sensitive to softwood species.

Table 3-3 Bonding stiffness of the glue lines for different clamping pressures

Species	**Clamping pressure (MPa)**	**Stiffness (N/mm^3)**
Spruce-Pine-Fir	0.1 MPa	19.0
	0.4 MPa	20.6

3.2.2.4. Coordination System and Wood Grains

In the modeling procedure, Cartesian coordinate system was used as the global coordinate system. If the cross layer ring orientations were to be considered, a polar orthotropic modeling method should be involved. However, it is not practical to record and monitor the ring orientation of each member in a cross layer; this aspect was not considered in this study. It should be noted that the coordination system in ANSYS should not be compared with the fiber directions, namely the longitudinal, tangential and radial directions. The coordination system is universal for this model, while the fiber directions alter by layers.

3.2.2.5. Determining the Load

To determine the center-point load in this model, tests data was used from Chapter 4. Based on the tests of 90 specimens of Hem-Fir 5-layer CLT specimens with clamping pressure of 0.1 MPa, the average ultimate load was 19.33 kN. In this simulated model, a load of 20 kN was used to study the failure behaviors and stress distribution of the members in the CLT cross-layers.

3.2.3. Analysis Methods

To study the failure mechanism of CLT cross-layers, information of individual node was first extracted from the established model. The information extracted from each node included the node coordination and the normal and shear stresses. For each single node, the stresses associated with its original global coordinate system were transformed with Mohr's circle analysis method to reveal the normal and shear stresses in different inclined planes. The result from analysis was then pooled for conclusions regarding the failure mechanism of CLT cross-layers.

3.2.3.1. Nodal Selection and Stress Information Extraction

After running the ANSYS model, the first step was to extract stresses from individual nodes that represent the stress distributions in cross-layers. Figure 3-4 indicates six nodes where information was extracted from this model.

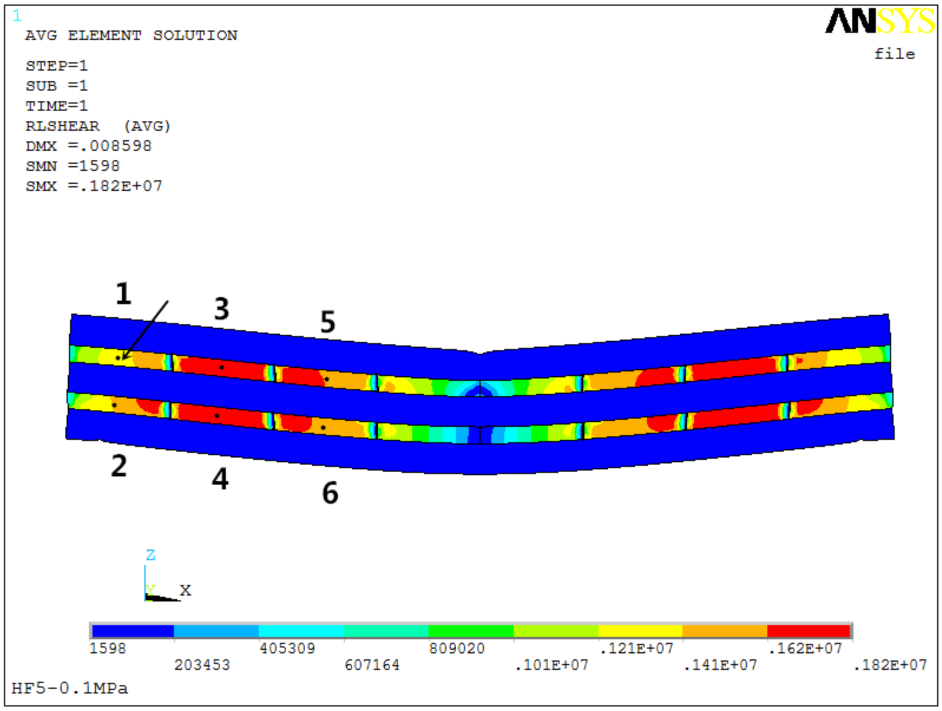

Figure 3-4 Information from six nodes extracted for analysis. Black dots indicate the position of each extracted node. The node numbering is also shows above or below each node.

Since this model has eight boards in each cross-layer, the symmetrical design allows point analysis on only one side of the beam. As Figure 3-4 shows, six individual nodes were selected as each node is the geometrical center of a cross-layer board. These six boards also represent the most frequent failure locations found in testing. The boards in the center were not considered in the analysis since they often remained intact in tests. The stress information including each node's normal stresses and shear stresses were extracted from ANSYS output for further analysis.

3.2.3.2. Mohr's Circle Analysis

Since the model established was using Cartesian coordinate system, the output from ANSYS analysis only provides stresses information which corresponding to the assumed coordinate, namely, the normal stresses in X and Z axes, and the shear stresses accordingly. However, to analyze the overall stress distribution of each selected node, the coordinate system needed to be rotated to obtain the normal and shear stresses at any inclined plane.

One simple way to obtain stresses at inclined planes is by introducing the Mohr's circle method. The Mohr's circle is one effective way to transform stresses with geometrical representations. This graphical analysis of stresses was first developed by a German civil Engineer, Otto Mohr, in the year of 1882. With the stress information given at any plane, this Mohr's circle can be plotted to give the stress transformation at any inclination or rotation. Figure 3-5 shows the plane rotation and stresses transformation.

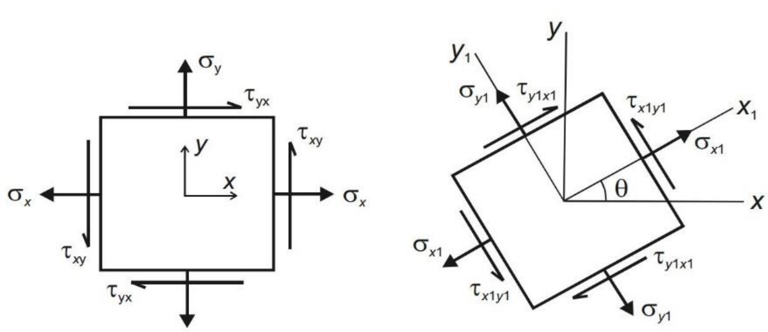

Figure 3-5 Stress transformation example: original stresses and stresses at an incline plane with θ degrees of rotation. (Image source: Autodesk Simulation Mechanical)

The left image of Figure 3-5 can be assumed as the original coordinate which the model was established in. At any inclined angle from the original plane, as the right image indicates, the stresses are changing with the rotation of the plane. Mohr's circle analysis provides the ways to transform the stresses among various planes of rotation.

The equation for a Mohr's circle is as follow.

$$(\sigma_{x'} - \sigma_{average})^2 + \tau_{x'y'}{}^2 = R^2 \qquad \text{Equation 3-1}$$

In this equation, $\sigma_{x'}$ and $\tau_{x'y'}$ represent the stresses after rotation of the plane. The center point of the circle is ($\sigma_{average}, 0$) and the radius is R, which are calculated as Equation 3-2 and 3-3.

$$\sigma_{average} = \frac{\sigma_x + \sigma_y}{2} \qquad \text{Equation 3-2}$$

$$R = \sqrt{(\frac{\sigma_x - \sigma_y}{2})^2 + \tau_{xy}{}^2} \qquad \text{Equation 3-3}$$

With these given equations and the original stress information from ANSYS output, this Mohr's circle can be plotted to show how normal stresses and shear stresses change as the plane rotated.

Figure 3-6 below shows an example of a Mohr's circle. Several terminologies should be clarified here for further model analysis.

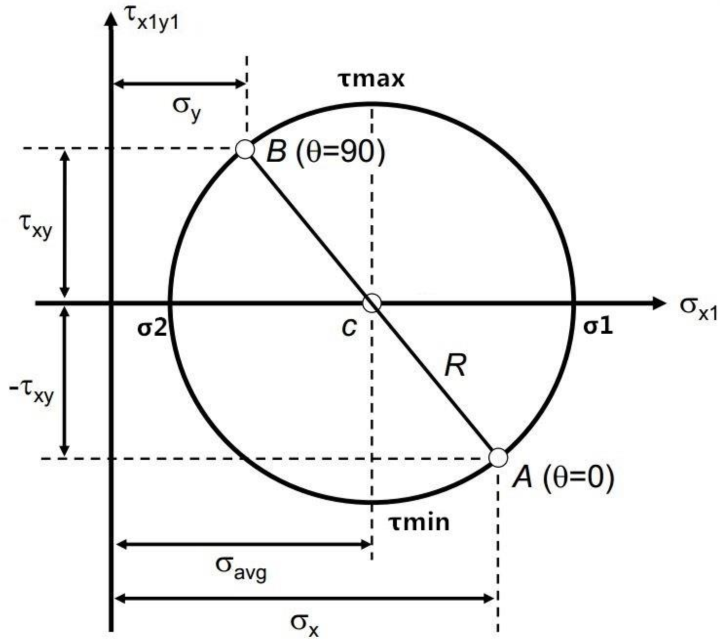

Figure 3-6 A sample of Mohr's circle. (Image source: Autodesk Simulation Mechanical)

As Figure 3-6 shows, in this sample Mohr's circle, the center point C has coordinate ($\sigma_{average}, 0$), while R is the radius of this circle. Point A on this circle shows the normal stress in x-direction and the shear stress at the original plane. Equation 3-2 can transform the normal stress in x-direction to calculate the normal stress in y-direction. On the abscissa, σ_1 and σ_2 give the principal stresses where the normal stresses in the x-direction reach extreme values. In the shear stress direction, $\tau_{\max}$ and $\tau_{\min}$ show that at these points, the shear stresses are maximized or minimized. Each point on this circle is corresponded to a rotated angle from the original plane.

In this situation, since the selected points are on the left side of this model, rotations of 30°, 45°, 60° and 90° will be used to calculate the stresses on these planes. The results of these changing stresses will be compared among different angles of rotation to elucidate the failure mechanism of CLT cross-layers.

3.3. Results and Discussion

In this section, the CLT model constructed in ANSYS was introduced. The coordinates of the selected nodes were then given, along with the stress information from ANSYS output. Mohr's circle analysis was performed where the normal stresses and shear stresses were observed as they changed with plane rotations. The possible failure modes and failure mechanism of CLT were given as the conclusion of this chapter.

3.3.1. CLT Model Presentation

With 20,000 N center-point loading on this beam, the ANSYS rolling shear stress output was shown in Figure 3-7. This is the simulated model for CLT 5-layer Hem-Fir specimen with manufacturing clamping pressure of 0.1 MPa. The cross-layers were plotted with color maps which showed the rolling stress gradient. The red colored areas are subjected to higher shear stress perpendicular to grain.

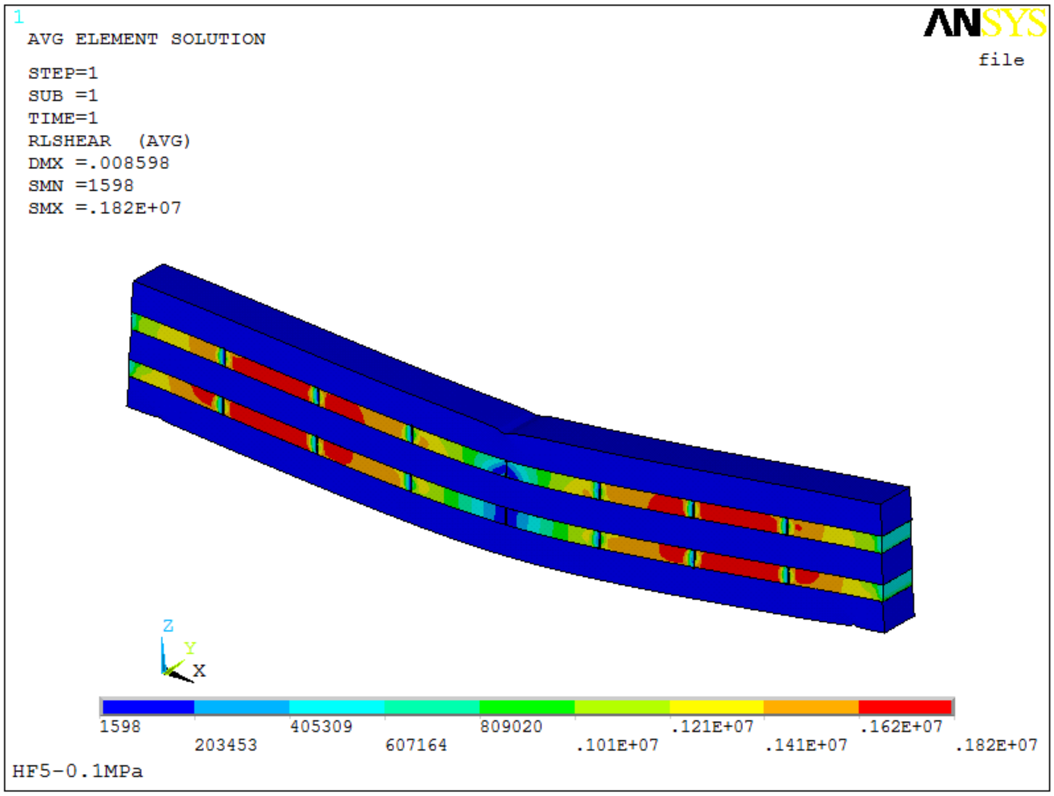

Figure 3-7 ANSYS model of CLT 5-Layer Hem-Fir specimen with clamping pressure of 0.1 MPa. The color map shows the rolling shear stress distribution of the cross-layers of this CLT beam. All numbers from the color map are in Pascals.

From Figure 3-7, it can be observed that the biggest vertical deformation happened at the loading point at the center of this beam. The gradient color maps in the cross layers gave the rolling shear stress distribution. As the red color indicated higher shear stress in the radial-tangential plane, the peak rolling shear stress was 1.82 MPa. It was observed that higher rolling shear stress was located in the second and third board in cross-layers from either end of this beam. The boards closed to the beam center and at both beam ends were under smaller shear stress as green and yellow color indicated.

It should be noted here that the rolling shear stress in Figure 3-7 only refers to shear stress in the X-Z plane of the cross layers in the Cartesian coordinate system in which this model was constructed. The X-Z plane in cross-layers was the radial tangential plane of the wood. All stress information in rotated plane will be obtained in the following sections.

3.3.2. Nodal Selection and Stress Results

As mentioned in section 3.2.3.1, six different nodes were selected. These nodes were all located in the geometrical center of each board selected. Table 3-4 shows the selected nodes and their coordinate in this model.

Table 3-4 Nodes selected and their coordinate information

Node	Node Number	Coordinate (in meter)		
		X	Y	Z
1	49595	0.0569	0	0.0965
2	36995	0.0569	0	0.0435
3	51170	0.1715	0	0.0965
4	38570	0.1715	0	0.0435
5	52745	0.2858	0	0.0965
6	40145	0.2858	0	0.0435

The post-processor in ANSYS gives the normal stresses and shear stresses output for these selected nodes. Table 3-5 shows all the stress information of these six nodes. These stress information will be used to construct Mohr’s circles to graphically represent stress transformation in the following section.

Table 3-5 Stress information for selected nodes in original ANSYS coordination system (All units are in Pascals)

Node	Node Number	Normal Stress			Shear Stress		
		S_X	S_Y	S_Z	S_{XY}	S_{YZ}	S_{XZ}
1	49595	-167520	-9825.8	-571120.0	-516.8	-13013.0	-1343300
2	36995	-390110	-24082	-1478100.0	-3104.7	-14463.0	-1479500
3	51170	-116290	-1937.7	-6539.5	-111.5	4418.5	-1702600
4	38570	75904	2158.7	49556.0	-592.3	6118.4	-1707800
5	52745	-190110	-3378.7	-582.7	466.7	9050.4	-1610000
6	40145	173040	4519.8	89721.0	33.6	10495.0	-1574400

3.3.3. Mohr's Circle Analysis

To demonstrate how stresses change on different rotated planes, Mohr's circle method was used in this section. As mentioned above, the Mohr's circle is an effective way to learn how normal stresses and shear stresses change when the plane on which the stresses act is rotated. To obtain Mohr's circles, the centers of the circles and radii were calculated according to Equations 3-2 and 3-3. Table 3-6 lists all the average normal stress ($\sigma_{average}$) and Mohr's circle radii (R) for these six nodes selected.

Table 3-6 Average normal stress and radii for six selected nodes

Node	Node Number	$\sigma_{average}$ (Pa)	R (Pa)
1	49595	-369320.00	1358373.34
2	36995	-934105.00	1576340.96
3	51170	-61414.75	1703484.09
4	38570	62730.00	1707850.81
5	52745	-95346.36	1612786.45
6	40145	131380.50	1574951.07

The center and radius information of node No.3 can be used to draw the Mohr's circle for the stress transformation. Totally there are six Mohr's circles for the six selected nodes. The detailed explanation of this method will be focused on node No.3 since the rolling shear stress from ANSYS simulated model is very high around this area, making node No.3 more typical for the failure mode analysis. Figure 3-8 gives the Mohr's circle of node No.3.

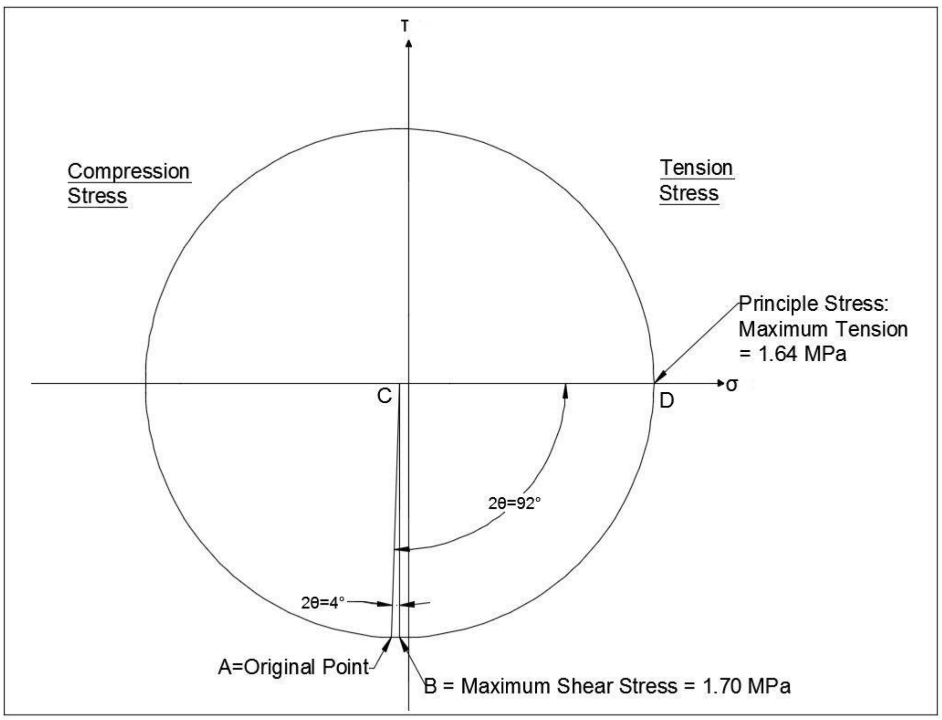

Figure 3-8 Mohr's circle of selected node No.3. The horizontal axis represents the normal stresses, and the vertical axis represent shear stresses. This circle gives an effective way to study the transformation of normal and shear stresses on various planes

Figure 3-8 shows this Cartesian coordinate system with the abscissa of normal stress and the ordinate of shear stress in the x-z plane. The abscissa's positive direction refers to tension stress while the negative direction means compression stress. The ordinate also shows positive and negative shear stresses as shown. The x-z shear stress gives the rolling shear stress according to the ANSYS coordinate system used. The circle shown in Figure 3-8 has center point C (-61414.75, 0) and radius of 1703484.09 according to the calculated results from Table 3-6. All numbers are in Pascals.

In Figure 3-8, point A on this circle indicates the original stress output from ANSYS model. This point A was located with the normal stresses and shear stresses of node No.3 given in Table 3-5. The shearing stress acted on point A, where the original plane of this node was 1.7 MPa. This amount of shear stress is closed to the maximum shear stress where point B indicates which was about 1.703 MPa. The calculation of the maximum shear stress was as shown below as Equation 3-4.

$$\tau_{\max} = \sqrt{(\frac{\sigma_x - \sigma_z}{2})^2 + \tau_{xz}{}^2} = \sqrt{(\frac{(-116290Pa) - (-6539.5Pa)}{2})^2 + (1702600Pa)^2} = 1.703MPa$$

Equation 3-4

At point A a small compressive stress also exists in the x-direction. It means at the original plane, this node was under a large shear stress with some minor compression stresses. In term of failure, shear stress would be acting alone to cause horizontally shear along the x-axis. As such one would expect the failure plane to be parallel to the x-axis (i.e. horizontal).

The rotation of the original plane can be represented by geometrical angles between two points on the Mohr's circle. The direction of rotation on the circle was consistent with the rotation of the plane, while the degree of rotation is only half of that of the angle presented on the circle. While the Mohr's circle provides geometrical relationships between the normal stress in x-axis and the shear stress in x-z plane, the next point of interest of Figure 3-8 was the point D. As it was shown in the figure, point A was rotated 92° to point D, where the principle stress presented the maximum tension stress of 1.64 MPa. The calculation of the principle stress is shown below as Equation 3-5.

$$\sigma_{\text{principle}} = \frac{\sigma_x + \sigma_z}{2} \pm \sqrt{(\frac{\sigma_x - \sigma_z}{2})^2 + \tau_{xz}{}^2} = 1.642MPa / -1.765MPa \qquad \text{Equation 3-5}$$

The maximum tension stress was calculated as 1.642 MPa. As for point A and D, the original plane of point A was rotated counterclockwise for half of 92°, which was 46°. Point D shows that if the plane of this node were rotated 46° counterclockwise, the shear stress in x-z plane would reach zero, while strong tension stress in x-axis would act on this node. In this situation, the cross-layer would fail at about 45° counterclockwise plane with tension stress pulling the fiber apart, with no contribution from the shear stress as it reached zero at this plane.

One interesting observation from laboratory tests is that most of the so-called "rolling shear" failures in CLT are typically at about 45° angle to the x-axis. However, since the principle stress only represents one specific rotated plane, this observation of ≈45° failure plane still cannot verify that tension stress is the sole reason for failure. The area of the Mohr's circle of point D's vicinity should be studied, instead of a simple point D. The parts of the circle above and below point D showed the presents of both shear stress and tension stress. In this area, the material had a strong tensile stress pulling it apart on the x-axis, while at the same time, shear stress shearing it apart on the x-z plane. This combined stresses with interactions between them was the actual failure mechanism of CLT cross-layers. Meanwhile, this combined state of stresses at point D also explained the angle of rolling shear failure cracks which were typically about 45° to the original axis.

In a brief conclusion, the Mohr's circle of node No.3 in Figure 3-8 shows that the cross-layer of CLT is likely to fail due to either the strong shear stress around the original axis, or a combined state of both shear and tension stresses at about 45° rotation from the original axis. If it failed according to the latter scenario, the reason of failure can be either tensile stress or shear stress. The true failure mode should only be known if the moment of failure initiation can be observed.

3.3.4. Tension Failure and Rolling Shear Failure

Traditionally, the cross-layers of CLT was believed to have the weakest material capacity because of the low rolling shear capacity of the radian-tangential plane. With the Mohr's circle method conducted in the last section, the tensile stress which maximized at about 45° plane also contributes to the failure of CLT cross-layers.

Materials fail when the stress acted on it goes beyond the material intrinsic strength. While the strength of the CLT specimen is not known, both rolling shear strength and tension perpendicular to grain strength are very small compared to their strengths in parallel to grain direction.

In the ANSYS model, six selected nodes and their Mohr's circles analysis are shown in Figure 3-9 as followed. In these six circles, most of the selected nodes had maximum tensile stress along the x-axis at about 45° plane rotated counterclockwise. In the vicinity of the principle stress point on Mohr's circles, shear stress in x-z plane was also presented in combination with the tensile stress perpendicular to grain.

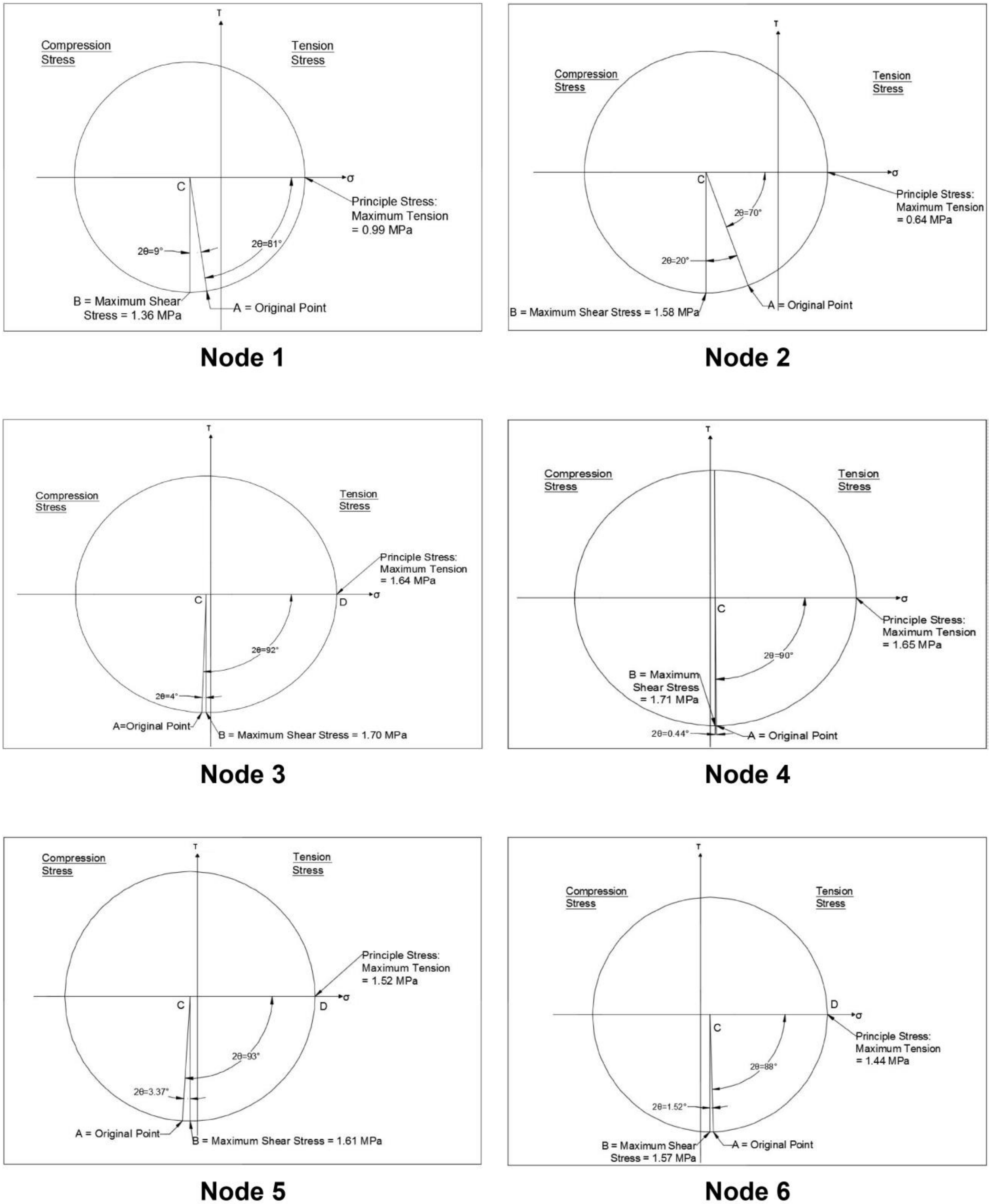

Figure 3-9 Six selected nodes and their Mohr's circles. For most of these nodes, the tensile stress in the x-direction is close to the maximum tensile stress between 35° and 50° plane rotated counterclockwise.

As Figure 3-9 shows, the rotations to the principle stress where tension was maximized ranged from 35° to 50° of all six selected nodes. In term of the stresses, the tensile stresses at point D of node 3 and node 4 were greater than other nodes, which showed that failures are more likely to happen on these two cross-layer components.

The Mohr's circle analysis showed that the cross-layers of CLT possibly possess two types of failure modes, the rolling shear failure and tensile perpendicular to grain failure. Between 35° and 50° counterclockwise rotation of the original plane, material is not only under shearing stress but also having large tensile stresses pulling it apart. The combination effect of these two types of stresses is likely to reduce both of the material strength, causing premature failures in CLT cross-layers.

Based on the observations and results from laboratory bending tests of CLT specimens, most of the failures in CLT cross-layers happened with cracks located at about 45° plane. The combination of shear and tensile stresses weakened the material strength, especially on rotated planes between 35° and 50°. With both rolling shear and tensile perpendicular to grain stresses acting on the cross-layer of CLT, the initial failure type of the material determines the failure mode of each CLT specimen. Proper testing monitoring tools should be used.

3.3.5. Conclusions

The 5-layer CLT Hem-Fir 0.1 MPa ANSYS model was loaded at 20,000 N under center point bending tests. The software output shows high rolling shear stress level on cross-layers, especially the boards closed to the center between the beam end and the loading point. To study the failure mechanism of CLT cross-layers, Mohr's circle analysis was conducted on six selected nodes from six cross-layer boards. Each node was interpreted as a Mohr's circle to learn the stress transformation on different planes. It shows that between 35° and 50°, each node was not only subjected to rolling shear stress, but also to a large tension perpendicular stress which was pulling the material apart. The combined effect of two different stresses weakened the material capacity. In terms of failure types, the initial failure in the cross-layers determines if it's a rolling shear failure or a tension perpendicular to grain failure.

4. Mechanical Testing of CLT Specimens

4.1. Introduction

Exact failure mechanism of the CLT cross-layers under out of plane bending loadings is very complicated and difficult to observe because the initiation of failure happens within microseconds. To better study the failure mechanism of CLT, center-point bending tests were set up in UBC Timber Engineering and Applied Mechanics (TEAM) Laboratory. Two different types of CLT panels, formed with pressing pressure of 0.1MPa and 0.4MPa, were used to prepare specimens. Three different loading rates were considered for the mechanical tests on CLT specimens.

To capture the initiation of failure in each test, a high speed camera was employed during the testing. Movies and images provided ample amount of evidence that the cross-layers failures of CLT were not only caused by shear stresses, but also tensile perpendicular to grain stresses that applied at an angle between 30 to 60 degrees to the longitudinal axis of the beam specimen. The new knowledge from the discovery of the significant influence of tensile perpendicular to grain stresses in the CLT cross-layers elucidates the “Rolling Shear” failure mechanisms that might lead to methods to improve the material performance.

4.2. Materials and Methods

4.2.1. Materials

The test material was obtained from left over prototype test materials from a previous project at UBC TEAM Laboratory TEAM 2011-01 (Yawalata, 2011). According to the project plan, Hem-Fir (H-F) CLT specimens were manufactured with second growth BC coastal Hemlock species. It is worth to mention the nomenclature of the species group Hem-Fir represents mostly a combination of Western Hemlock (*Tsuga heterophylla*) and Amabilis Fir (*Abies amabilis*) (Western, 1979). The harvesting sites and processing mills of these two species are normally mixed together to form the commercial species group Hem-Fir. Hem-Fir is one of the most important species groups in Canadian wood industry due to a wide range of uses and applications. Although named as Hem-Fir, in the testing concerned with this experiment, only Western Hemlock laminae were obtained to manufacture CLT panels.

These laminae were obtained from another TEAM project (TEAM 2009-03) where Hemlock lamina of 30.2 mm thick, 117.6 mm wide and 4000mm long, were produced. The average moisture content of the laminae was 12.9%. Grading of the laminae was performed by a certified grader. Also the flatwise modulus of elasticity of each lamina was measured by a Metriguard Model 340 E-Computer. Two different grades were assigned to these laminae where the average MOEs for Grade L_1 and L_2 are 13.9 GPa and 12.0 GPa, respectively.

5 Layer CLT panels were made from these Hem-Fir laminae. First, all of the laminae were planed down to 115 mm wide and 27 mm thick. Second, laminae were laid up side-by-side to form the first layer of the panel. Third, fast-cure Poly-Urethane adhesive was applied to the face of the lamina layer. Fourth, the next layer of lamina was laid on top of the previous layer with the member aligned perpendicular to the last layer. The lay-up and glue application process was repeated until 5 layers of laminae were formed. Lastly, the panels were press-cured for 40 minutes with two different pressures, i.e.: 0.1 MPa (14.50 psi) and 0.4 MPa (58.02 psi). The adhesive was applied at the rate of 160 g/m^2, and the number of replicates for each pressure was 3 panels. Figure 4-1 shows that the outmost layers are from Grade L_1 and three layers in the middle are from Grade L_2.

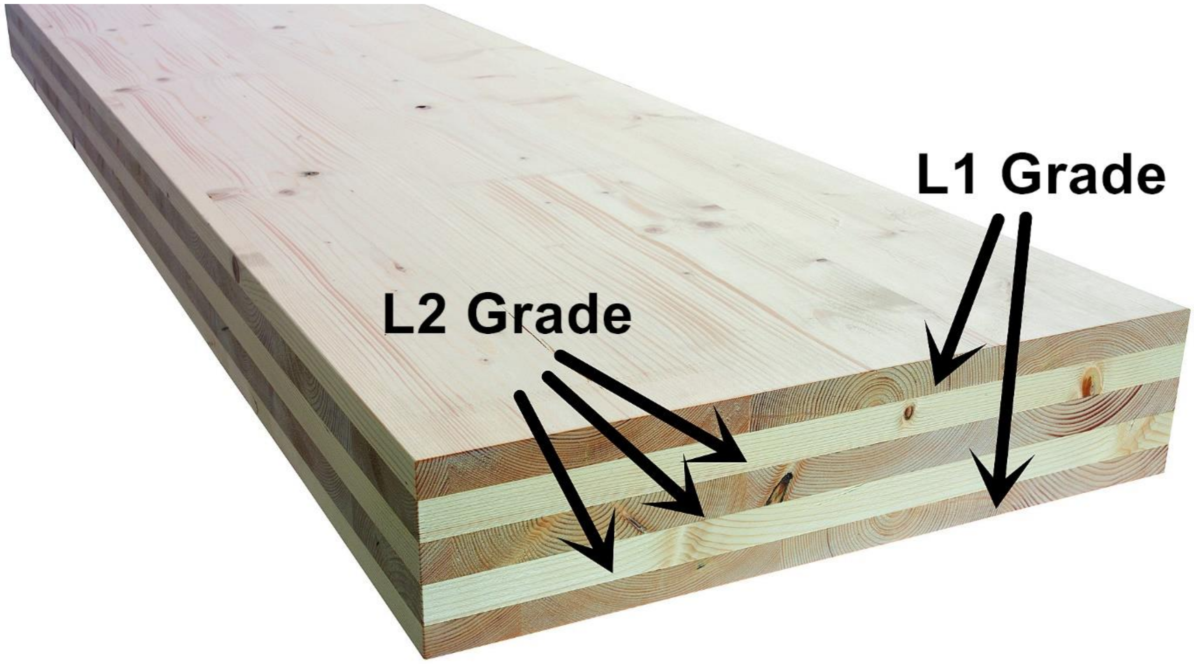

Figure 4-1 Grades of panels used to manufacture the CLT panels. The outmost layers are made from L1 grade panels, while three layers in the middle were made from L2 grade panels. (Image source: HYBRiD Build Solutions)

By the end of the CLT fabrication process, six 5-layer CLT Hem-Fir panels with average dimension of 140 mm x 1219.2 mm x 4000 mm were prepared with three replicates for each curing pressure. Smaller dimension specimens were then prepared from each panel for further experimental use.

4.2.2. Materials Preparation

Out of the six fabricated CLT panels as mentioned above, three were used in this part of the project including two H-F panels made under 0.1 MPa curing pressure and one H-F panel made under 0.4 MPa curing pressure. To best observe the effect of rolling shear failure in CLT cross-layers, the span-to-depth ratio was set to 6. Due to reasons such as the size of the testing machine, the limit of the cutting equipment and a sufficient sample size out of these three panels, the sample dimensions were set to 140 mm x 50.8 mm x 914.4 mm per specimen. In total two 0.1MPa CLT panels yielded 93 specimens and the 0.4 MPa panel yielded 60 specimens.

The panels were made to a final moisture content of 12.9% as stated before. The 153 specimens were further kept in the TEAM laboratory for over two months to reach equilibrium conditions. The specimens' moisture contents were measured with a hand-held double-pin type wood moisture meter. Table 4-1 shows the final dimensions and moisture contents of these 153 specimens.

Table 4-1 Specimens dimensions weights, and moisture contents

Specimens	Statistics	Width (mm)	Depth (mm)	Weight (g)	Moisture Content (%)
H-F 0.1MPa (93 Specimens)	Mean	50.92	137.50	3260.07	9.51
	Standard Deviation	0.51	0.46	78.83	1.01
	C.O.V.	1.00%	0.33%	2.42%	10.67%
H-F 0.4MPa (60 Specimens)	Mean	50.93	137.46	3257.39	9.30
	Standard Deviation	0.29	0.42	117.96	1.07
	C.O.V.	0.57%	0.31%	3.62%	11.52%

Based on the sample sizes of 93 and 60, these statistics are within acceptable range. Due to the relative lower relative humidity in the TEAM laboratory, the average moisture content of specimens is lower than the panel moisture content which was 12.9%. Although moisture content does affect material properties to some extent, it is assumed that the difference within each specimen group is small enough to neglect the impact of the small difference in moisture change on a brittle strength property.

Finally, vertical reference lines were marked on the specimen with pencils with 12.7 mm (0.5 inches) spacing. These lines aid the determination of failure modes during analysis of the images of the failure captured by the high speed camera. Figure 4-2 shows the reference lines system used in the testing.

Figure 4-2 Reference lines system used in the testing. The pencil lines marked on the side of the specimen from top to bottom has offset of 0.5 inches. These lines aid the determination of the initial failure mode during analysis of the images captured by high the speed camera.

4.2.3. Testing Set-up

4.2.3.1. Testing Standards

The center-point loading bending tests conducted in this study generally follow ASTM D198 – 14 (ASTM Standard D198-14, 2014).

4.2.3.2. Testing Machine

The testing machine used in this study is the universal Material Test System Model 810 located in the TEAM laboratory. The bearing plates provides support of the specimen at the given span, and a downward load which increases at a prescribed rate at the center of the beam. Under this center-point load, the section of the specimen between two supports can deflect without any restraint. The loading head is designed wider than the thickness of the specimen to avoid high stress concentration of the impact area. Machine operations were controlled by the console and the computer connected to this machine.

4.2.3.3. Modulus of Elasticity (MOE) Tests and Deflectometer

The first part of each specimen’s tests is non-destructive center-point bending test that gives material data for calculating the MOE. To obtain more accurate data on the deflection of the beam at the center point, a “Deflectometer” or called a Linear Voltage Displacement Transducer (LVDT) is fixed at the geometrical center point on the side of the beam. During each test, the LVDT measures the relative displacement between the center line of the beam at mid-span and the support. The data collected from both the transducer and the testing machine will be combined into calculations of the MOE of each beam. In MOE tests which are non-destructive, specimens are loaded up to only 3,000 N which stays within the material's elasticity range. This means when the force is removed after testing, the material is elastic enough to recover to its original geometry without any permanent tissue damage.

4.2.3.4. Ultimate Load Tests

The ultimate load test is the second part of each specimen's tests which destroys the specimen to measure the ultimate load it is able to take before failure occurs. The test set-up is mostly the same with previous ones only without the displacement transducer installed. The force loaded on the specimen will increase at the same rate until specimen fails.

4.2.3.5. Failure Criteria

The MOE test will not concern any material failures. However, in ultimate load tests, the failure criteria need to be defined beforehand. When the load applied generates enough stresses which go beyond the material strengths, it fails. During the testing procedure, when load exceeded a certain level, cracks began to show in the specimen which means that the accumulated energy was being released inside the specimen. Afterward, the force applied on the specimen will increase again until more cracks occurred. This load drop repeated several times before the specimen is totally destroyed. The failure criteria adopted in this study was, whenever the force drop exceeded 5,000 N, this specimen is considered as failed. Since this study mostly concentrates on the initial failure mechanism of CLT cross-layers, the complete material failure is not required here. The load each specimen can take before the force drops more than 5,000 N is defined as the ultimate load in this case.

4.2.3.6. Loading Rate

The rate of loading is one of many programmable parameters on the testing machine. Normally, two types of loading rate control methods can be achieved from the testing machine, namely the load control method and the displacement control method. For the tests concerned, the displacement control method was adopted as the loading rate was controlled by the displacement of the hydraulic platform. In this study, to better understand the material failure mechanism under different rate of loading circumstances, three different loading rates were chosen. As the unit of loading rates for displacement method is millimeter per minute, in this study, three adopted loading rates are 2 mm/min, 20 mm/min and 40 mm/min.

4.2.3.7. High Speed Camera Video Capture

No matter how slow the loading rate is, the material failure instant is too quick to observe that everything happens within microseconds. To fulfill the purpose of this study, which is to study the actual failure mechanism of rolling shear failures in CLT cross-layers, a high speed camera (HSC) was utilized to record the failure moments. This camera was a Phantom brand HSC v211, which shoots black and white high speed videos with 500 x 500 resolutions. The maximum frame per second rate was used in the testing, which was 2000 fps. This means the camera was able to capture 2000 images within a second of time. With a tripod support, the camera system was set up to collect the failure instants of the specimens. Figure 4-3 shows the camera set-up. Figure 4-4 gives a general test set-up for the testing done in this study.

Figure 4-3 High speed camera set up. The camera was supported by a generic tripod. For better picture quality, the illumination was strengthened by a pair of halogen work lights as the yellow object in the image.

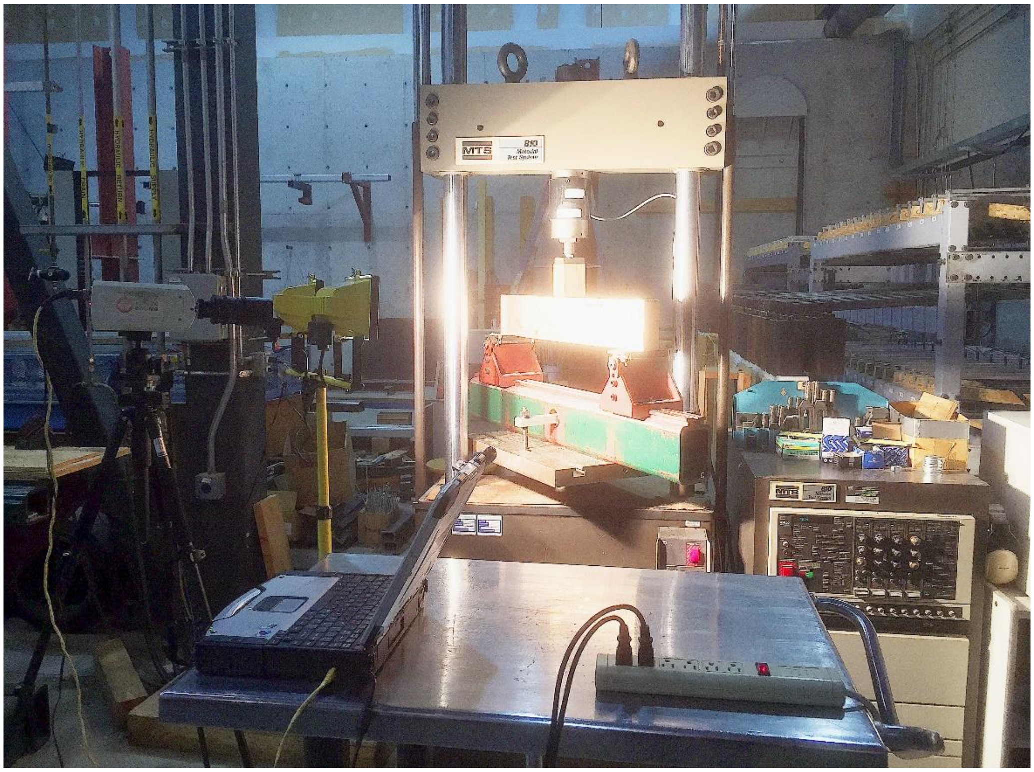

Figure 4-4 General test set-up. The testing machine platform was rotated to accommodate the angle of video shooting. The machine on the right side is the testing machine control console. The laptop is attached to the HSC for footage processing and storage.

4.2.4. Methods

As the MOE tests were the first part of this experiment, the data from machine readings and the transducer output were gathered. The MOE of each specimen was calculated for re-categorization. The MOE values of all specimens were ranked and categorized into different groups for further testing.

After the ultimate load tests were finished, the pooled data including machine output data, images and high speed camera video footages were processed for further analysis. The failure mode of each specimen was studied in details to examine the failure mechanism of CLT in terms of shear and tension perpendicular to grain failures.

4.2.4.1. Calculating the Modulus of Elasticity

The modulus of elasticity, also called the Young's modulus, is one of the most important material properties when it comes to the mechanical performances of a material. Under the testing condition mentioned above, center-point loading with two supports will place stress into the beam, thus causing the beam to bend. The deformation of the beam at the loading point is called the deflection. The elasticity of each material is determined by the modulus of elasticity while this value is the ratio of the stress placed on the beam to the strain resulted from the stress. From the stress-strain curve as Figure 4-5 shows, the modulus of elasticity is equal to the slope of the straight line section which indicates the pure elastic phase of the material.

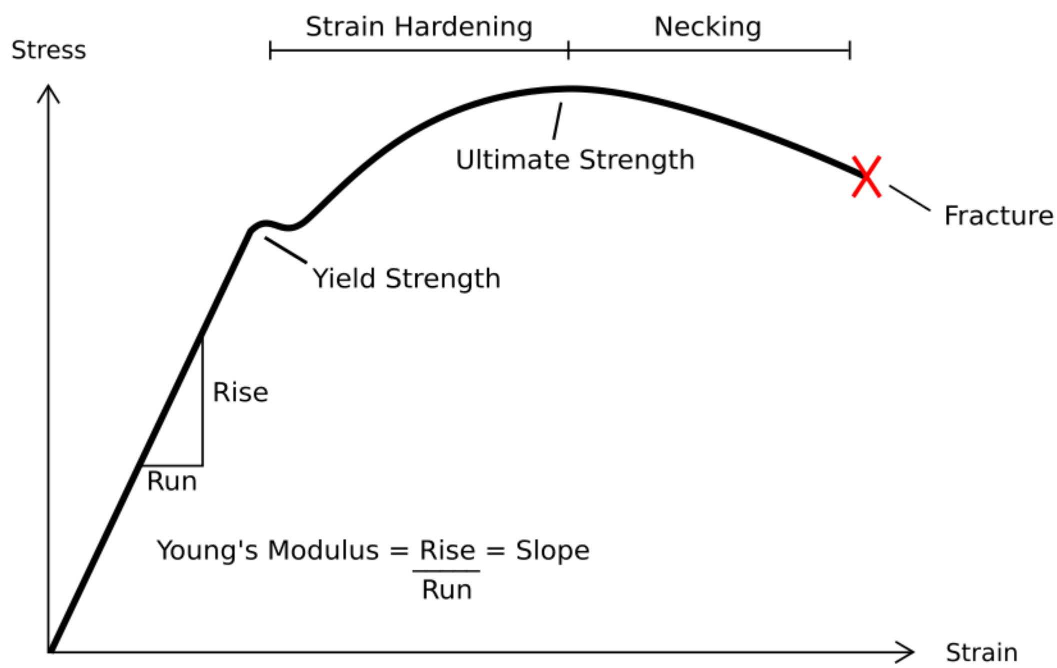

Figure 4-5 The stress-strain relationship for wood products. The slope of the elastic phase which is represented by the straight line on the left is the modulus of elasticity of this material. (Image source: Wikipedia)

For the calculation of the modulus of elasticity, the machine loading history and the exact deflection must be recorded during the tests. The testing machine’s console is able to record the loads history precisely. However, the deflection of the specimen must be measured with a transducer fixed at the center point of the neutral axis. According to ASTM D198 – 14, the MOE calculation can be manipulated to the following form as Equation 4-1.

$$E_{app} = \frac{Pl^3}{4bd^3\Delta} \qquad \text{Equation 4-1}$$

$E_{app} =$ Apparent modulus of elasticity

$P =$ Load change (N)

$l =$ Length of the specimen between two supports (mm)

$b =$ Width of the specimen (mm)

$d =$ Thickness of the specimen (mm)

$\Delta =$ Deflection change at the center point of the neutral axis (mm)

It is important to mention that this way of calculation gives the apparent modulus of elasticity only. The true modulus of elasticity cannot be calculated with this formula. In bending tests, the total deflection is the result from both of the bending deflection and the shear deflection. The true MOE is referred to the MOE without any shear deflection involved. The apparent MOE considers both of the bending and shear deflection at the same time. Since the purpose of calculating the MOE in this study is merely to re-categorize the specimens into groups, the apparent MOE sufficiently meet the demand here. For center-point bending tests and engineered wood product such as CLT, the true MOE requires further methods to calculate, which is not of interest here.

4.2.4.2. Specimens Re-categorization

After the completion of MOE calculations, all of the specimens were re-categorized into three groups according to the MOE values. Specimens were randomly ranked and re-grouped to achieve similar MOE mean values between groups.

This step was necessary and had the following rationales. First, there were three different loading rates as 2 mm/min, 20 mm/min and 40 mm/min. Specimens needed to be divided into groups for various loading rates. Second, the MOE re-categorization step purposely reduced the variations between groups of specimens. For instance, all 93 0.1MPa specimens were prepared from three panels where the defects and material properties might vary significantly between panels. The MOE re-categorization randomly grouped all the specimens into three groups to maintain similar MOE mean values between groups. This successfully minimize the variation between groups, thus, increased the comparability of data from different groups.

After re-grouping of specimens, there were 31 specimens in each 0.1 MPa group, totaling 3 groups with 93 specimens. For the 0.4 MPa specimens, all 60 were considered as one single group for further analysis.

4.2.4.3. Failure Mode Analysis

During the ultimate load tests, all of the specimens were loaded to failure. The failure mode, especially the initiation of failure is the interest of this study. The high speed camera images and testing data were combined to study the failure mechanism of CLT cross-layers. Various failure modes will be compared depending on the failure types including tension, shear or others.

4.2.4.4. Initial Failure Modes and Annual Ring Orientations

Observations from experiments showed that the failure cracks usually are tangential or perpendicular to the annual rings. The captured failures will be compared with the initial failure modes and the annual ring orientations to seek potential relationship between.

4.3. Results and Discussion

4.3.1. Modulus of Elasticity of Specimens

Specimens were tested for their modulus of elasticity at the first stage of the experiment. The MOEs were calculated with Equation 4.1 and ranked for re-categorization. For the 0.1MPa specimens which included 93 pieces, the apparent MOE calculation results are as shown in Table 4-2 and Figure 4-6.

Table 4-2 0.1 MPa 93 specimens MOE statistics

Specimens Group	No. of Specimens	Mean MOE (GPa)	St.Dev(GPa)	C.o.V
HF-5Layers-0.1MPa	93	4.68	0.44	9.49%

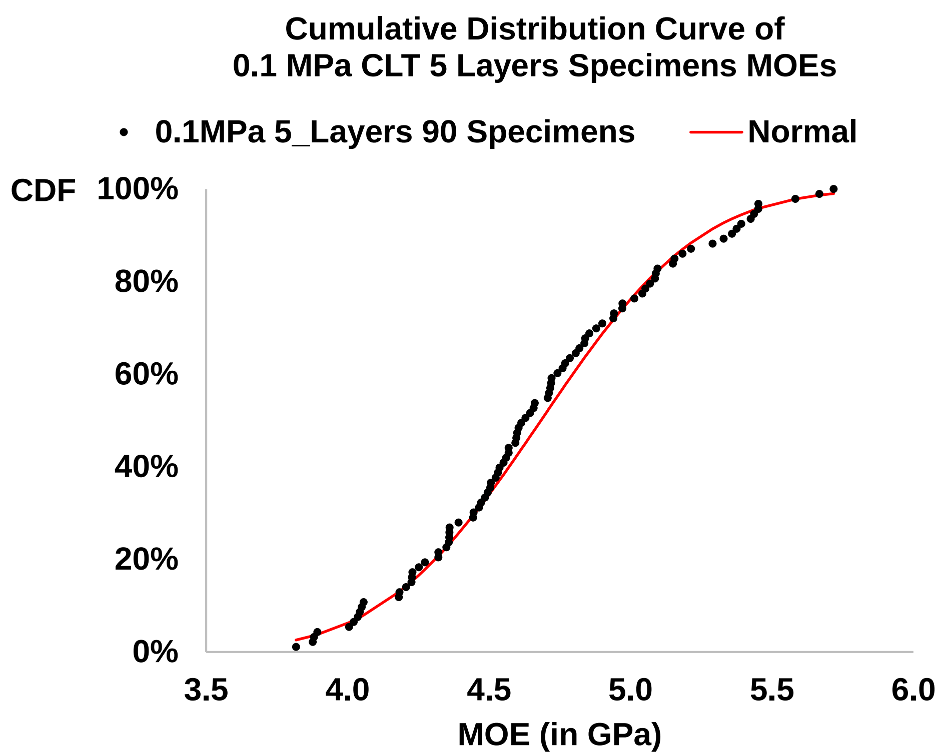

Figure 4-6 The cumulative distribution curve of the MOEs of 0.1MPa CLT specimens. It can be observed that the sample MOEs are follow the normal curve very well, showing good normality of sample statistics.

As Table 4-2 shows, for a sample size of 93, both of the standard deviation and the coefficient of variation are within range of acceptance. Although the MOE values of the original Hemlock panels used to manufacture these CLT beams were 13.9 GPa for L_1 grade and 12.0 for L_2 grade, the mean MOE for the CLT specimens calculated was 4.68

GPa which is much lower. This is due to the method of calculation of the apparent MOE which treated this engineered wood product of CLT as a homogeneous material. However, this way of calculation the MOE is still valid when ranking these values to re-categorize the specimens as the results are positively related to the real MOEs of these specimens. Other methods are available for the calculation of the real MOE value for composite beams such as CLT.

For the 0.4 MPa samples, the sample size was 60. Same MOE tests were conducted on these specimens. Table 4-3 and Figure 4-7 shows the MOE statistics and the cumulative distribution curve of the testing data.

Table 4-3 0.4 MPa 60 specimens MOE statistics

Specimens Group	No. of Specimens	Mean MOE (GPa)	St.Dev (GPa)	C.o.V
HF-5Layers-0.4MPa	60	4.76	0.47	9.90%

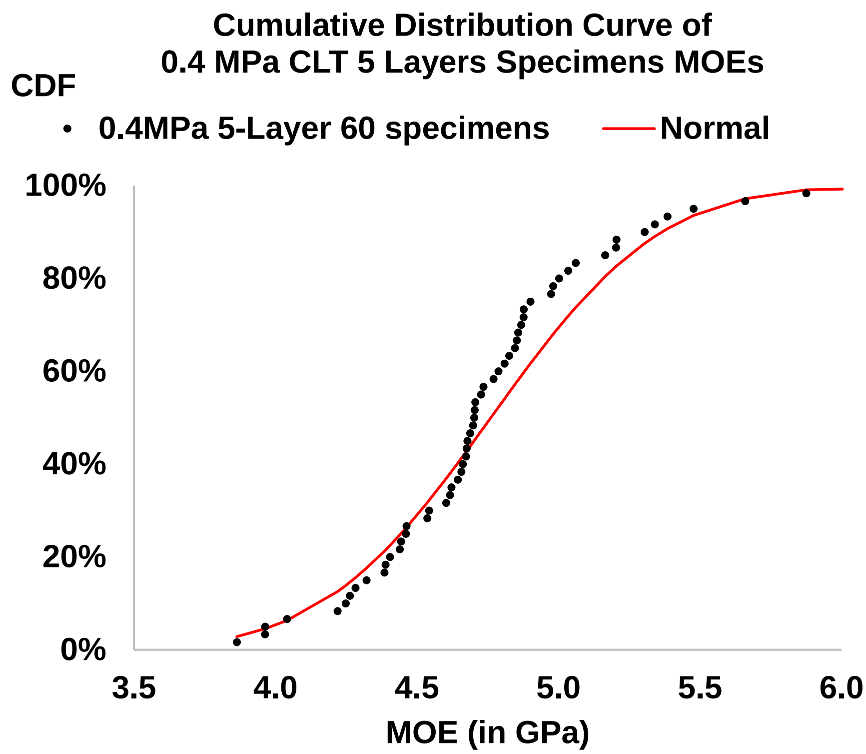

Figure 4-7 The cumulative distribution curve of the MOEs of 0.4MPa CLT specimens. Compared to CDF of 0.1MPa specimens, the mean value and the deviations of sample data are very close to Figure 4-6. It shows that specimens prepared from panels made under two different pressures are comparable.

In order to determine the comparability between the testing data from 0.1 MPa specimens and 0.4 MPa specimens, statistical tests were carried on the MOEs of two groups of specimens. Figure 4-8 shows the combines cumulative MOEs of both groups of specimens.

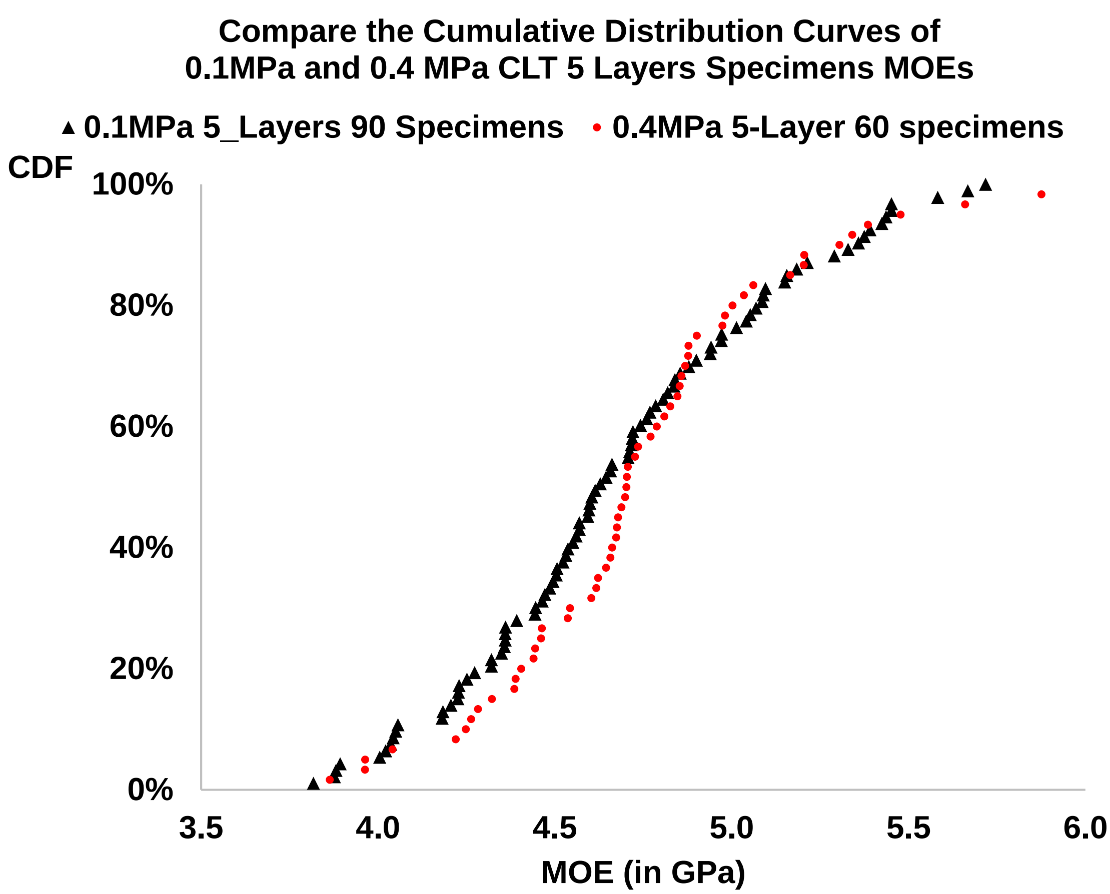

Figure 4-8 The cumulative MOEs of both 0.1 MPa and 0.4 MPa CLT specimens. Two groups of specimens have similar MOE distributions, while the red points, indicating the 0.4 MPa MOEs, are likely to have greater values than the black triangles. Further statistical tests are needed to determine how similar two groups of data are.

To compare the differences, statistical tests were conducted. In this case, since all the specimens are the ones will be tested on for further research, they can be considered as the populations. A t-test was conducted in this case, utilizing the following t-score calculation as Equation 4-2.

$$t = \frac{\bar{x}_1 - \bar{x}_2}{\sqrt{\frac{s_1^{\,2}}{n_1} + \frac{s_2^{\,2}}{n_2}}}$$

Equation 4-2

Table 4-4 shows the means and standard deviations of these two groups of specimens.

Table 4-4 0.4 MPa 60 specimens MOE statistics

	0.1 MPa Group	**0.4 MPa Group**
Sample Size	93	60
Mean (GPa)	4.68	4.76
St. Dev (GPa)	0.44	0.47
C.o.V	9.49%	9.90%

According to Equation 4-2, the calculated t = -1.01. The hypothesis was,

$$H0: \mu_1 = \mu_2$$
$$H1: \mu_1 \neq \mu_2$$
$$\alpha = 0.05$$

The next step is to look up $t_{59,0.025}$ in the t-table which gave a critical value of 2.00. The computed t of 1.01 did not exceed the tabled value, so the null hypothesis would not be rejected. In conclusion, it is very possible that, with the confidence of 95%, the MOE values of 0.1 MPa specimens are of the same average compared to the MOE values of the 0.4 MPa 5-layers CLT specimens.

4.3.2. Re-categorizing the Specimens of 0.1MPa CLT

For the 93 specimens that were made from 0.1 MPa Hem-Fir panels, 3 of them were used as trial pieces when the testing machine was set up for the ultimate load tests. The rest of 90 specimens were re-categorized according to the MOE values into three groups that the average MOE of each group are purposely controlled at a similar level. Three letters were assigned to each group as Groups S, M, and L. Table 4-5 shows the test data of three groups of specimens. Three groups have very similar means and variance in terms of MOE and ultimate loads.

Table 4-5 Test statistics of S, M, and L groups of 0.1 MPa specimens

Group		S Group	M Group	L Group
Sample Size		30	30	30
MOE	Mean (GPa)	4.63	4.73	4.69
	St. Dev (GPa)	0.45	0.46	0.44
	C.o.V	9.66%	9.67%	9.35%
Ultimate Load	Mean (kN)	18.18	19.84	19.98
	St. Dev (kN)	2.29	2.33	1.88
	C.o.V	12.62%	11.75%	9.39%

4.3.3. Testing Specimens under Different Loading Rates

As two different loading rates were used in the testing of 90 specimens of 0.1MPa CLT, Group S and M were chosen for a slower loading rate of 2 mm/min while Group L was loaded 10 times faster at 20 mm/min. The effect of loading rates was studied with testing data and statistics. Table 4-6 shows the testing results of specimens under two different loading rates.

Table 4-6 Test statistics of specimens under various loading rates

	Group S, M	Group L
Sample Size	60	30
Loading Rate (mm/min)	2	20
Ultimate Load (kN)	19.01	19.98
St. Dev (kN)	2.48	1.91
C.o.V	13.03%	9.55%

A t-test was used here to identify the difference between two means. The null hypothesis was as below while the significance level was set at 5%.

$$H0: \mu_1 = \mu_2$$
$$H1: \mu_1 < \mu_2$$
$$\alpha = 0.05$$

Calculations of the t value was as follow,

$$t = \frac{x_1 - x_2}{\sqrt{\frac{s_1^{\ 2}}{n_1} + \frac{s_2^{\ 2}}{n_2}}} = \frac{19008.36 - 19981.18}{\sqrt{\frac{2477.06^2}{60} + \frac{1908.34^2}{30}}} = -2.057$$

So the t-score was as calculated -2.057. The degree of freedom was set as the smaller sample size minus 1. So in this case the degree is freedom parameter is 30 – 1 = 29. Because the hypothesis was set as a one-tailed test, the alpha level of 0.05 remains in whole (If two-tailed test, the alpha level is usually divided into half). The critical t-value was obtained from a t-table, as,

$$t_{0.05,29} = 1.699$$

As the computed t-value (absolute value) of 2.057 had exceeded the critical t-value, we should reject the null hypothesis. The specimens loaded at 2 mm/min resulted in a slightly lower failure loads mean compared to ones loaded at 20 mm/min.

On the other hand, if a two-tailed t-test was conducted to look for difference between these two groups in either direction, then the controlled t-value was,

$$t_{0.025,88} = 1.987$$

Now the calculation of t-score was different from before. Firstly, assume that the variances in both groups were the same, that the difference between standard deviations was ignored. The pooled variance was calculated as,

$$S_p{}^2 = \frac{(n_1-1)s_1{}^2 + (n_2-1)s_2{}^2}{n_1+n_2-2} = \frac{(60-1)(2477.06)^2 + (30-1)(1908.34)^2}{60+30-2} = 5313912$$

$$t = \frac{\overline{x}_1 - \overline{x}_2}{\sqrt{s_p{}^2(\frac{1}{n_1}+\frac{1}{n_2})}} = \frac{19008.36 - 19981.18}{\sqrt{(5313912)(\frac{1}{60}+\frac{1}{30})}} = -1.8873$$

So this time the absolute value of the computed t-score was smaller than the critical t value of 1.987. Now accept the null hypothesis that two means were the same.

In conclusion, the hypothesis gave different results if different assumptions were made. If it was assumed that this was a one-tailed test which meant that by default, Groups S and M had lower mean than that of Group L, then the difference was significant between two means. On the other hand, if it was assumed that this was a two-tailed test, which meant that it was interested to compare two means assuming they were the same, then two means are the same from the hypothesis test, with 95% confidence interval given.

At 95% confidence level, faster loading rate is seemingly providing slightly higher ultimate loads for center-point bending tests. However, there is not enough evidence to quantify the relationship between loading rate and the ultimate load level with the tests done.

4.3.4. Initial Failure Modes of CLT Specimens

The failure mechanism of CLT cross-layers is a complex procedure that happens within a few microseconds of time. While traditionally believed that the rolling shear stresses are the major reason for cross-layers' failures, the results from finite element analysis using commercial software ANSYS gave different potentials claiming that the tensile perpendicular to grain stresses might also damage the cross-layers first before shear stresses cause the damage. Whichever happens first, the shear or tensile failure, the final massive failures occurred afterward are due to very complicated stress re-distributions. This means that the initial crack is what to look for in terms of the failure mechanism of CLT cross-layers.

To capture the initial, a high speed camera was incorporated into the experiment. This camera is able to record 2000 frames per second black and white video with 500 x 500 resolutions. Due to the equipment limit, only one side of the beam could be videoed, leaving the observation of failure less possible as the other side was not under video coverage. However, a number of successful initial failures were captured finally for further research and study.

Figure 4-9 below shows three adjacent images withdrawn from the video when the initial failure happened instantly. The specimen as shown was numbered as HF0.4-(3)-11, which was one of the 0.4 MPa specimens. The order to observe three images is from top to bottom with half microsecond time lapse in between. On image No.1, the cross-layers of the CLT beam were still good without any observable crack happened. However, in the middle image showing 0.5 microseconds after the first one, a small-scale fiber split was observed on the left side of the bottom cross-layers where the red box indicates. Last, on image No.3, this failure enlarged with displacement of the reference line as indicated in the red boxes in the pictures due to the radial-tangential shear stresses tearing the fiber horizontally.

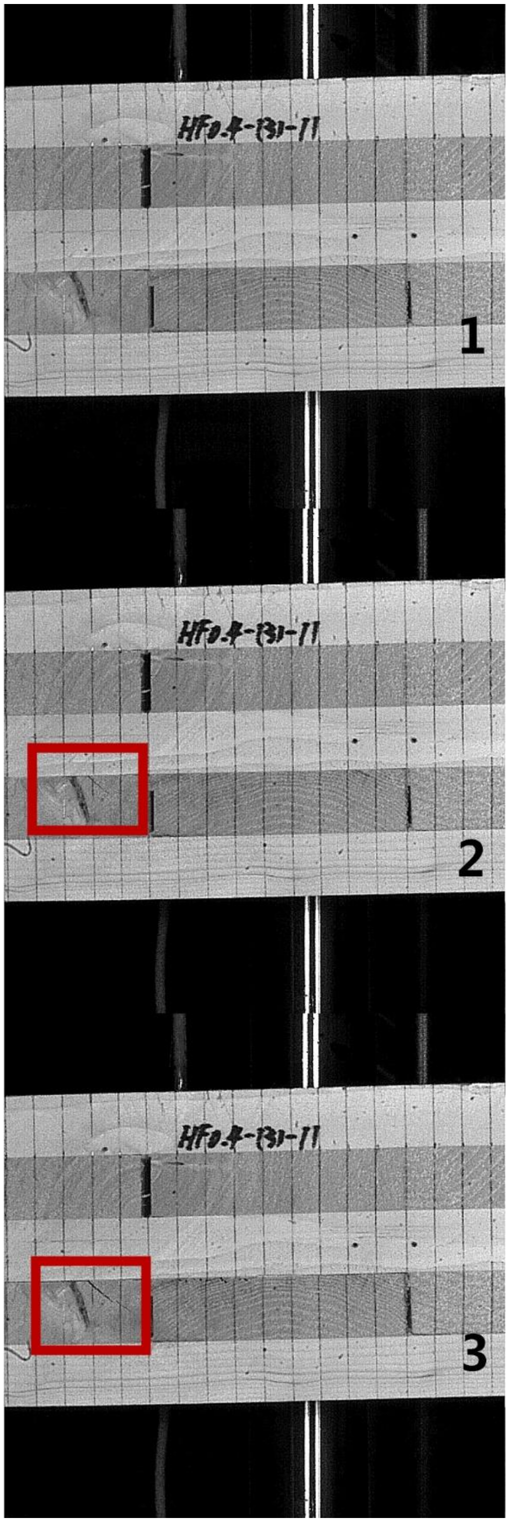

Figure 4-9 Three images of the specimen under center-point load. The time lapse between each neighbored image is 0.5 microsecond. The order to observe is from left to right.

As mentioned before, Examination of the images at the initiation of failure with the reference line system provides important evidence of the initial failure mode. For instance, in Figure 4-9, the reference line in the second image crossing the initial crack appears as straight as the one in the first image, implying that this initial crack was opened up by tension perpendicular to grain stresses. After the initial failure occurred, the redistributed stresses worked on the fiber with great complications, as the right side image showing obvious horizontal displacement along the reference line going across the crack.

The reference lines are an effective and time-saving system to decide the initial failure mode in the tests done within this study. The mechanism of fiber failure is that the stresses exceed the corresponding strength of the material. While various strengths of wood in the radial-tangential direction are different from each other, the initial failure must be due to one single type of stress, instead of the combination of various stress types. All of the initial failures can be categorized into three types, as,

1) Tension perpendicular to grain type initial failure

2) Rolling shear type initial failure

3) Marginal initial failure

Figure 4-10 gives the criteria to distinguish the types of initial failure between rolling shear and tension perpendicular to grain. If the reference line opens up without horizontal displacement observed, then it is defined as a tension perpendicular to grain type initial failure. Oppositely, as the right side image shows, if the line is obviously displaced along the crack, then rolling shear stress is the reason of this failure. However, if initial failure shows both rolling shear and tension perpendicular to grain failures, this specimen is grouped as the third group as a marginal type of initial failure.

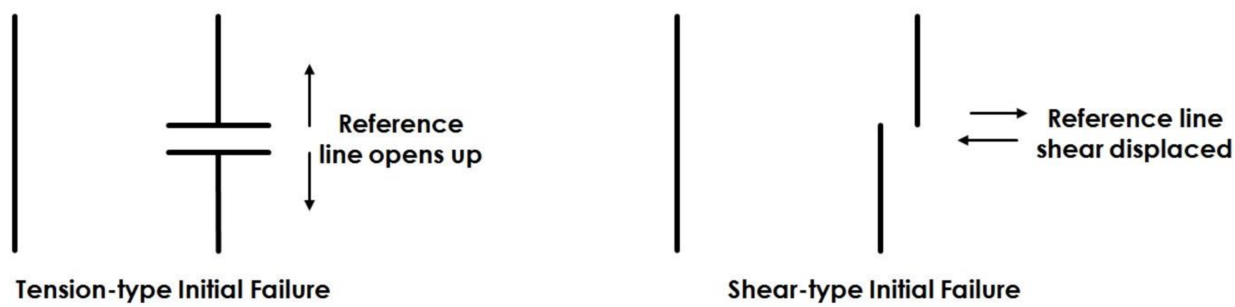

Figure 4-10 Reference line system and the way to distinguish the initial failure types between tension perpendicular to grain and rolling shear failures.

From Figure 4-10, the rolling shear failure and tension perpendicular initial failures can be distinguished by judging the displacement of the reference lines. However, during the experiment, the third group of initial failure which is the marginal ones is not rare at all. One situation is that multiple initial failures could occur at the same time, at least appeared to be at the same time due to the time lapse between frames is limited to 0.5 microsecond. When both rolling shear and tension perpendicular to grain initial failures are shown in the video, this specimen is regarded as a marginal failure sample. Another possible circumstance is also considered as a marginal initial failure, when the displacement of the reference line is too minimal to be observed in the picture.

CLT has weak cross-layers that limit the entire material performance. Under bending circumstances, the term of rolling shear failure is a bit misleading that one will think naturally that rolling shear strength is the governing property of the material. However, the testing shows that it is not always the case. Figure 4-11 gives another example of the tension perpendicular to grain type initial failure. Image No.2 indicates no displacement of the reference line along the cracks. This is suggesting that tension perpendicular to grain stress is the reason causing the initial failure of the cross-layers. After the initial failure appeared, as in image 3, displacement of reference lines can be observed showing stressed complication.

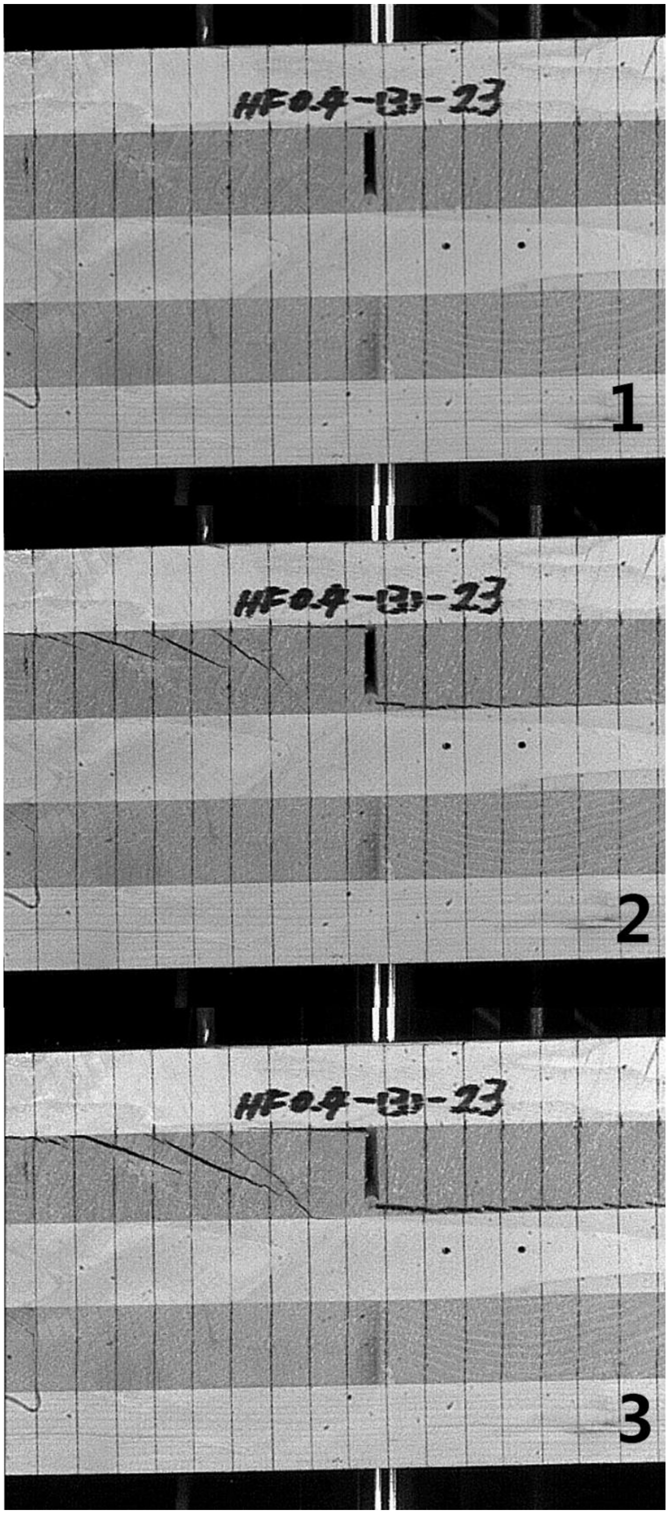

Figure 4-11 The initial failure instant of specimen HF0.4-(3)-23. It was considered as the tension perpendicular to grain type initial failure as well since no displacement was observed long the reference line in image 2.

The rolling shear type of failures was also observed frequently during testing. Unlike the tension perpendicular to grain type of failure, the initial failure was governed by radian-tangential shear stress for rolling shear type of failures. Figure 4-12 gives an example of the rolling shear failure in CLT cross-layers. The initiation of failure observed in image 2 shows obvious displacement along the crack. This displacement of the reference lines shows that shear stress might be the governing stress when material began to fail in the cross-layer of CLT. Although this type of failure can be regarded as rolling shear failure in CLT, the influence of the tension perpendicular to grain stresses cannot be ignored.

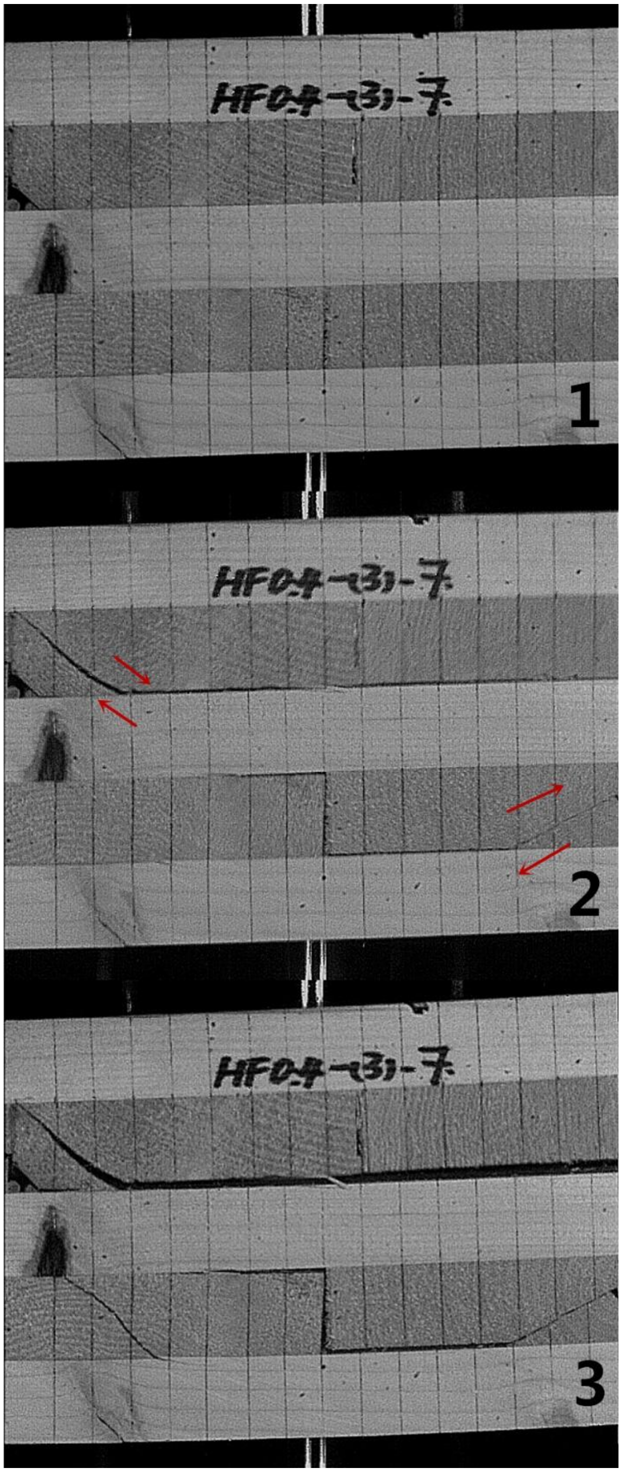

Figure 4-12 An example of rolling shear type of failures. The initiation of failure observed in image 2 shown as red arrows caused displacement along the crack. The displacement shows that shear stress governs the failure of CLT cross-layer in this case.

It is worth to mention that the failure cracks observed in the tests are very likely to be at an angle of 30 - 60 degrees from the longitudinal axis of the beam. This corresponds to the results of ANSYS modeling which indicated that the tension perpendicular to grain stresses are maximizing in the range of 30 - 60 degrees of rotation, influencing the overall capacity of the material.

The observation of the failure instants of CLT specimens with high speed camera backs up the determination of the failure mode. However, as the camera sacrifices image quality to capture more frames for slow motion, only one side of each CLT specimen was recorded for failure mode analysis. For the reason being, out of 153 samples, only 65 successful captured failure videos were obtained, while others failed on the other side that was not covered by the camera. The failure modes statistics for all 65 specimens are shown in Table 4-7.

Table 4-7 Failure modes statistics for specimens of which failure were successfully observed. 65 Specimens were included in this table. Most of the specimens failed in tension perpendicular to grain or rolling shear.

Failure Mode	No. of Specimen
Tension perpendicular to grain	26
Rolling shear	23
Marginal	16

From Table 4-7, it shows that the majority of specimens failed in tension perpendicular to grain type of failure or rolling shear failure. Rolling shear stress is not the only reason causing cross-layer's initial failure. As tension perpendicular to grain stress also exists in the failure plane, it is therefore an important failure factor to consider. Moreover, since the failure happened almost instantaneously, the time lapse between images of 0.5 microseconds may not be quick enough to capture the initial failure moment. This suggests that if a rolling shear initial failure was recognized based on the image evidence, there is a chance that the actual initial failure was still caused by tension perpendicular to grain stress during the 0.5 microsecond between two images. However, the converse is not true because if rolling shear failure occurred at first place, the lines would have displaced laterally before tensile opening appeared. Based on this hypothesis, the count of tension perpendicular to grain failures in Table 4-7 is possible greater while some rolling shear failures were actually not the case.

Considering the picture quality and frame rate of the camera, the marginal group reduces ambiguity when judging the initial failure type of specimens. As mentioned before, to avoid subjective judgments, the marginal initial failure group is used to categorize these specimens which cannot be judged as pure rolling shear or tension perpendicular to grain initial failure type. Figure 4-13 shows one specimen that was grouped as the marginal initial failure. Image 2 shows that both type of initial failure appeared in the same picture. The upper red arrow points to tension perpendicular to grain open-ups while the lower red arrow shows an example of rolling shear failure while displacement of the reference line is observed. To avoid ambiguity, this specimen is later grouped as the marginal type of initial failure.

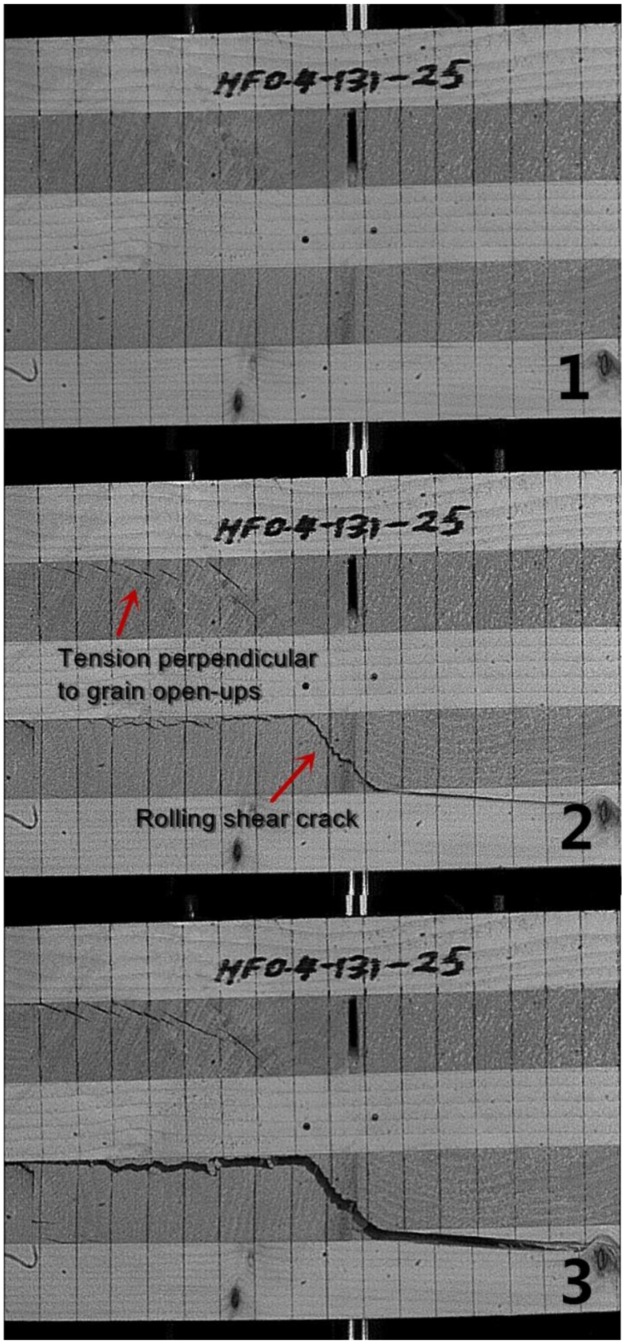

Figure 4-13 Specimen HF0.4-(3)-25 is grouped as a marginal initial failure. Image 2 shows both tension perpendicular to grain and rolling shear failures.

4.3.5. Faster Loading Rate and Initial Failures

As most of the specimens were loaded with 2 mm/min rate or 20 mm/min rate, 6 specimens were loaded with even faster loading rate of 40 mm/min. These tests were to be observed with high speed camera for the initial failure moments to discover any difference with slower loading rate specimens. Figure 4-12 shows the specimen numbered HF0.4-(3)-28 which was loaded at the rate of 40 mm/min.

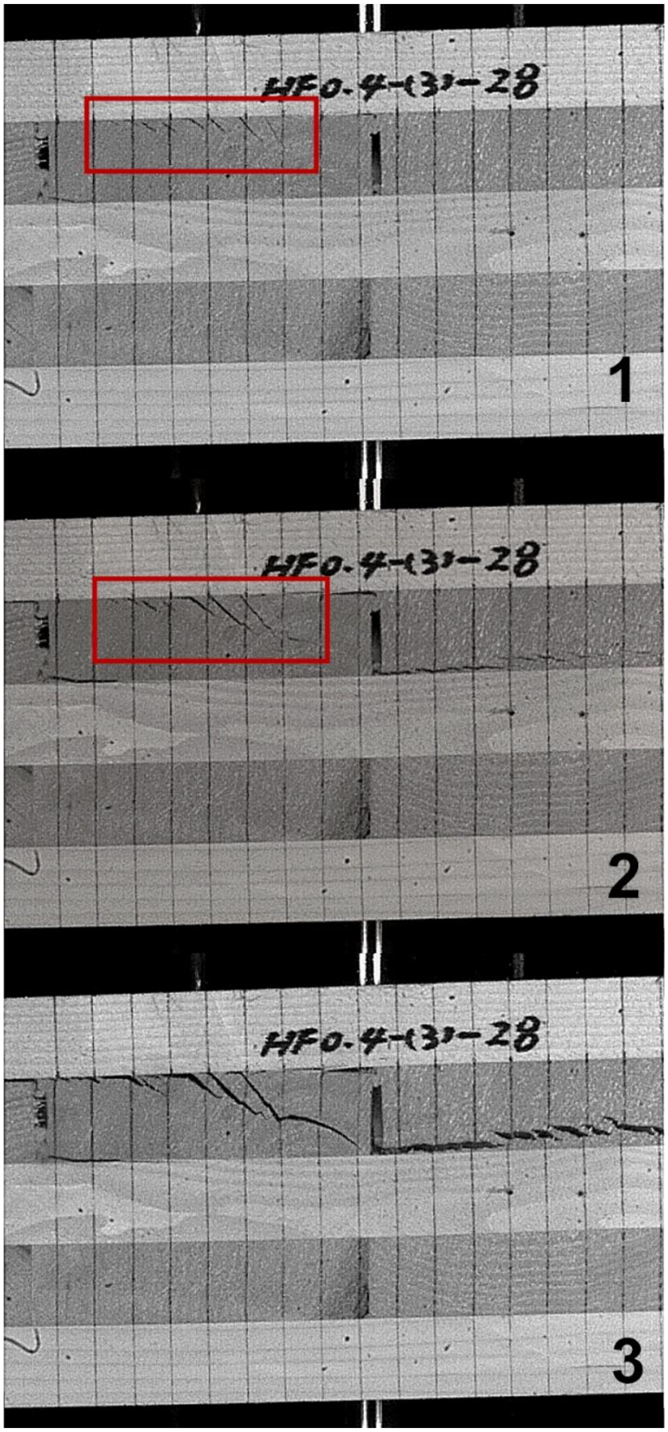

Figure 4-14 The initial failure instant of specimen HF0.4-(3)-28. The initial tension perpendicular to grain failure can be observed from the red box in image 1 where no displacement of the reference lines presented along the cracks. Images 2 and 3 shows the complication of failures after initial cracks happened, that the shear displacements can be easily seen on the pictures.

As Figure 4-12 shows, the initial failure mode of this specimen was tension perpendicular to grain type. Furthermore, all six specimens loaded with 40 mm/min loading rate were observed to have initial tension perpendicular to grain failures which means that the reference lines were straight immediately after initiation of failure. Figure 4-13 below gives another example that shows the initial tension perpendicular to grain failure clearly.

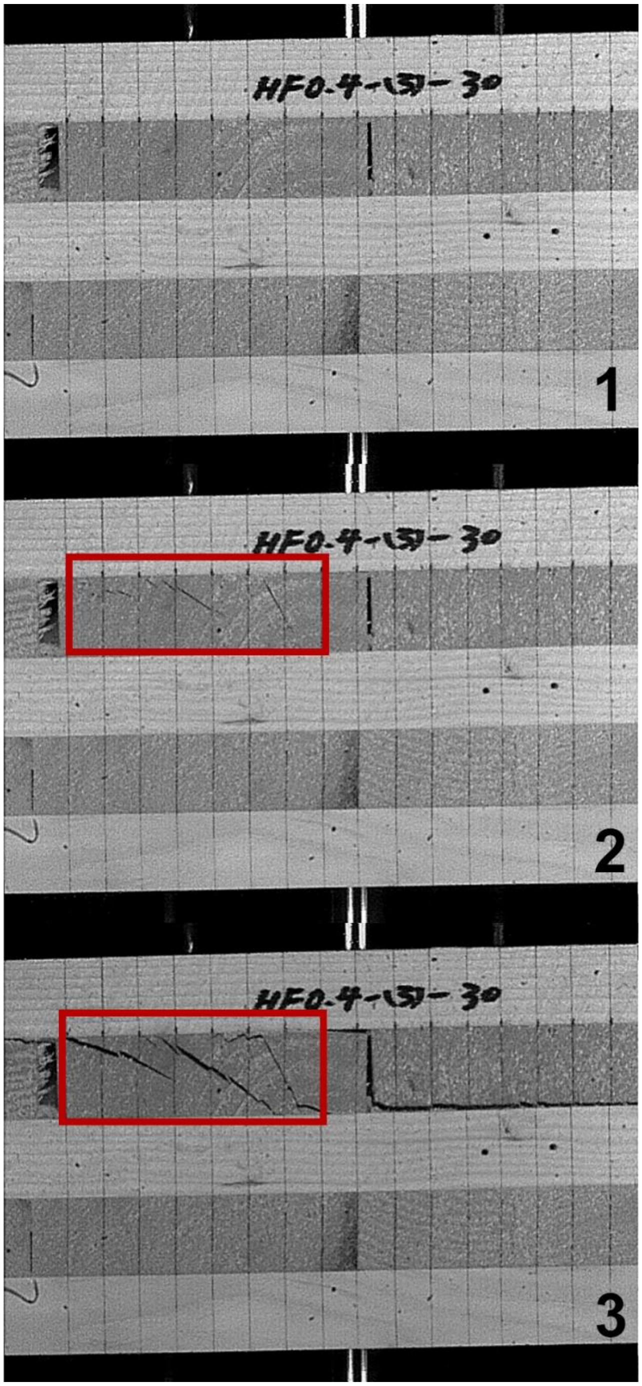

Figure 4-15 The initial failure instant of specimen HF0.4-(3)-30. Image 2 shows the initial cracks appeared in the red box. These failures were grouped as tension perpendicular to grain type initial open-ups as the reference lines were straight along the cracks.

Table 4-8 Comparisons of the test statistics of three different loading rates

<table>
<tr><th colspan="2">Loading Rate (mm/min)</th><th>2</th><th>20</th><th>40</th></tr>
<tr><td colspan="2">Sample Size</td><td>114</td><td>30</td><td>6</td></tr>
<tr><td colspan="2">Ultimate Load (kN)</td><td>19.76</td><td>19.98</td><td>21.55</td></tr>
<tr><td colspan="2">St. Dev (kN)</td><td>2.40</td><td>1.91</td><td>2.59</td></tr>
<tr><td colspan="2">C.o.V.</td><td>12.20%</td><td>9.55%</td><td>12.00%</td></tr>
<tr><td rowspan="3">Specimens Failure Mode Counts</td><td>Tension Perp. to Grain</td><td>14</td><td>10</td><td>2</td></tr>
<tr><td>Rolling Shear</td><td>16</td><td>7</td><td>0</td></tr>
<tr><td>Marginal</td><td>13</td><td>3</td><td>0</td></tr>
</table>

Table 4-8 shows the comparisons among test statistics of different loading rates. Despite the fact that only 6 specimens were loaded at the highest rate of 40 mm/min, the mean ultimate load of 21.55 kN is much higher than that of the lower rates of loading. Based on HSC videos caught on tape, most of the rolling shear failures happened when the loading rate is slow, while more tension perpendicular to grain failures were observed when faster loading rates were adopted. It can be prudentially concluded that when CLT beam is under high rate of loading which causes severe deflection change in a short time, the cross-layers of the CLT beam is more susceptible to be subjected to tension perpendicular to grain type initial failures. On the contrary, if the CLT beam is loaded at a slower rate, rolling shear failures are more likely to be the initial failure type in cross-layers. Meanwhile, higher the rate of loading is, the CLT specimens show higher capacity to center-point loads. The higher rate of loading is likely to be closer to reality since load controlled method is adopted in reality rather than displacement controlled method used in this experiment.

4.3.6. Initial Failure Modes and Annual Ring Orientations

During the experiments, it was observed that the failure crack direction was normally either tangential to perpendicular to the wood annual ring orientations. This section will combine the initial failure modes and the failure crack's direction with the annual ring orientations to seek possible relationships in between.

Generally, for the 65 specimens with captured high speed camera videos and images, there are three types of failure crack directions to the annual ring orientations. Figure 4-16 shows these three types of failure cracks according to their angles with the annual rings. Type A refers to the failure cracks which were tangential to the annual ring orientations. Type B refers to the failure cracks which were perpendicular to the annual ring orientations. Type C includes all other failure crack orientations that could not be grouped to either Type A or B.

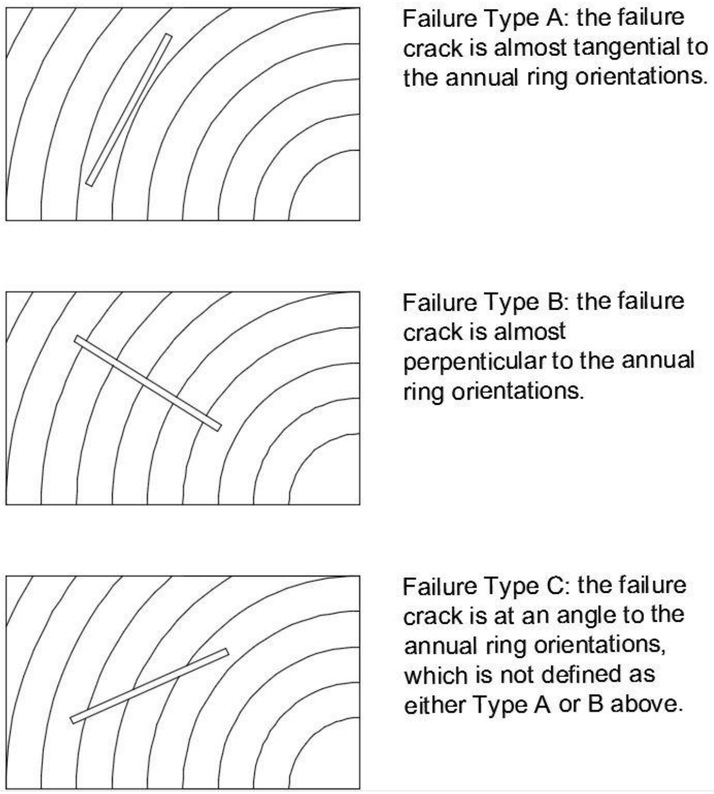

Figure 4-16 Three types of failure cracks according to angles with the annual ring orientations.

Among all 65 specimens which had successful failure instants captures, the failure crack and grain angles of Types A, B and C are grouped as the following Table 4-9 shows.

Table 4-9 Statistics of 65 specimens by their initial failure modes and the crack-to-grain angle type

Failure Mode / Crack and Annual Ring Angle	Type A	Type B	Type C	Total
	Tangential	Perpendicular	In between	
Tension perp. to grain	0	22	3	26
Rolling shear	7	12	5	23
Marginal	1	11	4	16
Total	8	45	12	65
Mean Ultimate Load (kN)	19.98	19.85	19.86	19.90

Among all 65 specimens, only 8 Type A and 12 Type C failure cracks were found. Figure 4-17 and 4-19 gives images for these two types of failures.

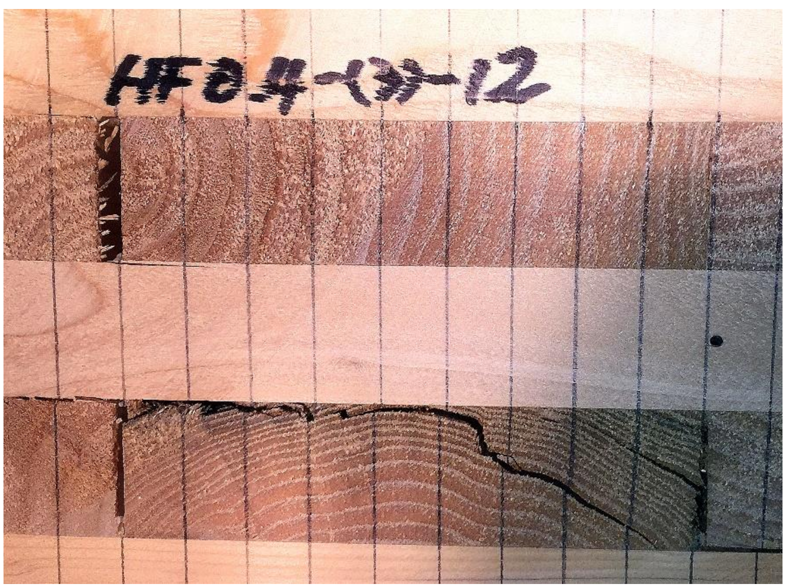

Figure 4-17 An example of Type A failure from specimen HF-0.4MPa-(3)-12. The failure crack went tangential with the annual rings. The initial failure mode for this specimen was the rolling shear failure.

Table 4-9 reported the mean ultimate load for each type of failure mode. The mean ultimate loads of three types of failure modes are almost of same level, where no difference was observed.

From Table 4-9, 8 specimens were recorded as Type A failure where the initial failure crack split along the annual ring directions parallel. Among these 8 specimens, 7 of them were categorized as rolling shear failure mode, indicating very high possibility that rolling shear stress sheared in the parallel direction with the annual rings which caused Type A cracks. None of the Type A failure was accounted for tension perpendicular to grain stress, showing that the density gradient between early wood and late wood is more susceptible to rolling shear stress parallel to annual rings, instead of the tension stress perpendicular to the annual rings.

As Table 4-9 shows, 45 out of these 65 specimens had Type B failure crack to annual rings angles, which was the perpendicular type. As there were 22 specimens observed without reference line movement, the tension perpendicular to grain type of crack was observed most frequently in the experiment. Figure 4-18 gives exemplary photo for this type of failure crack. On the other hand, rolling shear and marginal types of failures appeared 12 and 11 times, showing these two failure modes are less likely causing radial cracks in CLT cross-layers.

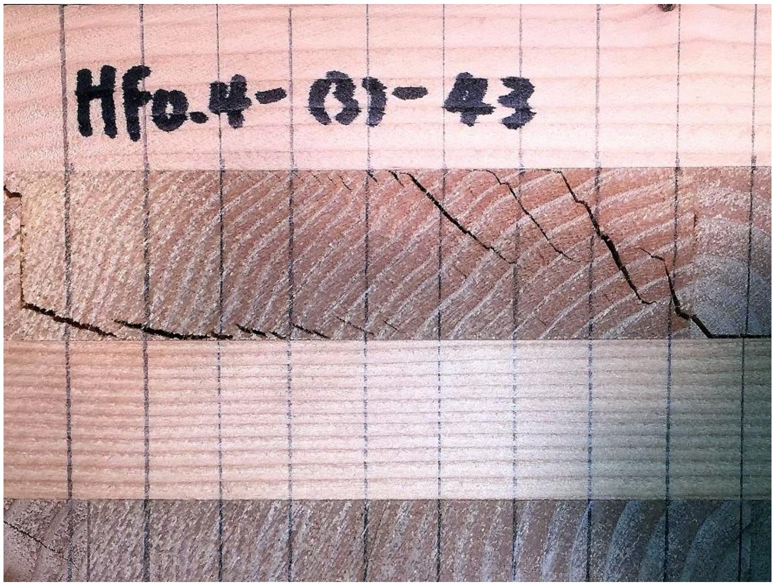

Figure 4-18 An example of Type B failure from specimen HF-0.4MPa-(3)-43. Multiple failure cracks were perpendicular to the annual rings' orientation. The initial failure mode of this specimen was tension perpendicular to grain failure.

Figure 4-18 shows the failure cracks of specimen HF-0.4MPa-(3)-43. This specimen was recognized as a tension perpendicular to grain initial failure. All of the failure cracks, as shown in the image, were perpendicular to the annual ring orientations.

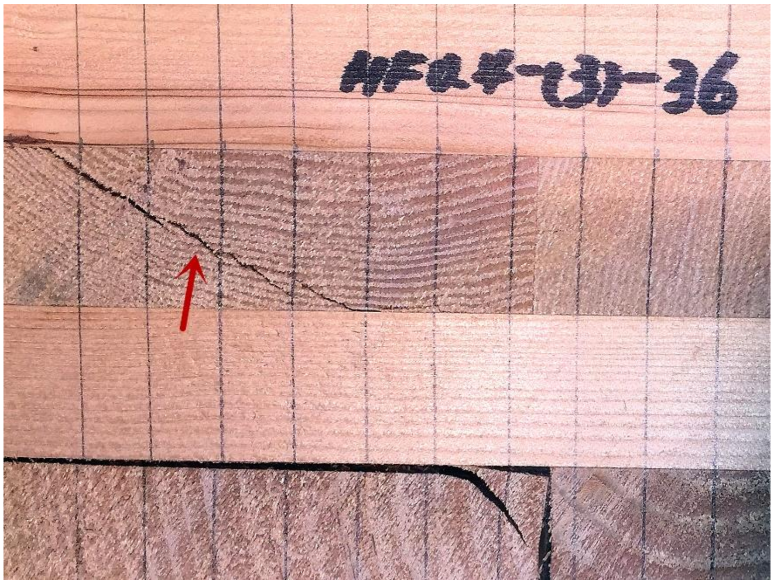

Figure 4-19 An example of Type C failure from specimen HF-0.4MPa-(3)-36. The failure crack shown by the red arrow in the image has an angle with the annual ring orientations. This type of failure is regarded as the intermediate type between Type A and Type B.

The data above shows that since most of the specimens had failure crack perpendicular to the annual ring orientations, it is very likely that tension perpendicular to grain stress caused failures perpendicular to wood grains. As wood grains contain early wood and late wood, the latter one has much higher density compared to early wood. The initial failure of Type A failure is likely to be caused by rolling shear stress since density gradient between early wood and late wood is more likely failed by shear stress tangential to the grains. On the other hand, if Type B failure happens that the crack goes perpendicular to the wood grains, it is more likely that tension perpendicular to grain initial failure takes place as it pulls the grains apart. The Mohr’s circle analysis from Chapter 3 also suggested that around 45° rotated plane, strong tension stresses were found. Since there are 45 specimens were found as Type B failure, the finding reinforces the concept that tension perpendicular to grain stress is an important factor affecting the failure of CLT cross-layers.

4.4. Conclusions

CLT specimens were tested non-destructively for MOE values at first. The re-categorization of 0.1 MPa specimens into three groups obtained similar group means in terms of MOE values. Two different types of specimens, including 0.1 MPa ones and 0.4 MPa ones, were tested and compared with statistical tests in terms of MOE values. Statistical tests showed that there is no different between the MOE of two groups of specimens. The ultimate load tests data were compared between two different loading rates of 2 mm/min and 20 mm/min. Statistical tests shows that the ultimate loads of specimens loaded at the faster rate of 20 mm/min have a slightly higher mean, compared to that of the specimens loaded at 2 mm/min. The tests done on six specimens loaded at the even higher rate of loading of 40 mm/min also supports that specimens have higher capacity of load when loaded at faster loading rates.

The high speed camera videos provided an effective way to study the initial failure moment of the specimen. Traditionally, shear stress was believe to cause the rolling shear failure in the cross-layers of CLT beams. However, it was observed that the initial failure in the cross-layers can be caused by many different reasons. Both rolling shear and tension perpendicular to grain stresses can trigger the initial crack in the cross-layers. The reference line systems allow the initial failure type to be distinguished from images captured by the high speed camera. This provides evidence that the tension perpendicular to grain stress is an important factor that causes material failure under center-point loads.

Last but not the least, it was concluded that most of the failure cracks were perpendicular to the annual ring orientations. It shows that the ring orientations in CLT cross-layers are related to the failure pattern. When transformed rolling shear stresses are tangential to the annual rings, the density gradient makes it more susceptible to shear failure. On the other hand, if transformed rolling shear stresses are perpendicular to annual rings, large tension stresses around 45° rotated plane more likely cause initial failures.

5. Conclusions and Recommendations

5.1. General Conclusions

As one of the latest engineered wood products, CLT, as a timber material with many advantages, has its wide range of uses in building constructions. Due to the design of orthogonally alternating laminates, the mechanical performance of CLT cross-layers is significantly governed by its low rolling shear capacity. This research focused on the failure mechanism of CLT cross-layer and its relation to rolling shear stress.

Computer finite-element modeling of 5-layers Hem-Fir CLT model was established in this research. The model specimen was loaded at 20,000 N under center-point bending condition. The results showed high rolling shear stress level on cross-layers, especially boards closed to the center between the beam end and the loading point. To study the failure mechanism of CLT cross-layers, Mohr’s circle analysis was conducted on six selected nodes from six cross-layer boards. The stresses of each node were interpreted as a Mohr’s circle to learn the stress transformation on different planes. It showed that between 35° and 50° plane rotations, each node was not only subjected to rolling shear stress, but also to a large tension perpendicular stress which also possibly cause material tensile failure. The combined effect of two different stresses weakened the ultimate material capacity. In terms of failure mechanism, the initial failure in the cross-layers was determined by either rolling shear stress or tension perpendicular to grain stress.

CLT specimens were tested non-destructively for MOE values at first. The re-categorization of 0.1 MPa specimens into three groups obtained similar group means in terms of MOE values. Two different types of specimens, including 0.1 MPa ones and 0.4 MPa ones, were tested and compared with statistical tests in terms of MOE values. Statistical tests showed that there is no different between the MOE of two groups of specimens. The ultimate load tests data were compared between two different loading rates of 2 mm/min and 20 mm/min. Statistical tests shows that the ultimate loads of specimens loaded at the faster rate of 20 mm/min have a slightly higher mean, compared to that of the specimens loaded at 2 mm/min. The tests done on six specimens loaded at the even higher rate of loading of 40 mm/min also supports that specimens have higher capacity of load when loaded at faster loading rates.

The high speed camera videos provided an effective way to study the initial failure moment of the specimen. Traditionally, shear stress was believe to cause the rolling shear failure in the cross-layers of CLT beams. However, it was observed that the initial failure in the cross-layers can be caused by many different reasons. Both rolling shear and tension perpendicular to grain stresses can trigger the initial crack in the cross-layers. The reference line systems allow the initial failure type to be distinguished from images captured by the high speed camera. This provides evidence that the tension perpendicular to grain stress is an important factor that causes material failure under center-point loads.

Last but not the least, it was concluded that most of the failure cracks were perpendicular to the annual ring orientations. It shows that the ring orientations in CLT cross-layers are related to the failure pattern. When transformed rolling shear stresses are tangential to the annual rings, the density gradient makes it more susceptible to shear failure. On the other hand, if transformed rolling shear stresses are perpendicular to annual rings, large tension stresses around 45° rotated plane more likely cause initial failures.

5.2. Recommendations for Further Research

The weak rolling shear properties of CLT cross-layers have been regarded as the factor which governs the mechanical capacity of CLT. However, this research shows that tension perpendicular to grain stress also contributed to the failure. The reality is that two stresses are working in a combined fashion at about 45° plane to cause material failure. Interaction of these combined stresses should be a subject of study.

Furthermore, this research only concentrated on 5 layer Hem-Fir CLT specimens, while variables may change such as number of laminates, species, span-to-depth ratio, and the cross-layers thickness. Similar research should be conducted to seek the failure mechanism of cross-layers of CLT specimens with different parameters. Moreover, different methods to reinforce the CLT specimens could be studied, especially ways to reinforce the materials in terms of the tension perpendicular to grain stress which lessened the material strengths in combination with the rolling shear stress.

Bibliography

Aicher, S. and Dill-Langer, G. (2000). Basic considerations to rolling shear modulus in wooden boards. *Otto Graf Journal, 11,* 157-166

ASTM, D4442-07. (2007). *Standard test methods for direct moisture content measurement of wood and wood-base materials*. ASTM International, USA.

ASTM, D0198-14. (2014). *Standard test method of static tests of lumber in structural sizes.* ASTM International, USA.

Biblis, E. (2000). Rolling shear modulus of sweetgum plywood and unidirectionally laminated veneer. *Wood and Fiber Science, 32,* 1, 2-6.

Ceccotti, A. (2008). New technologies for construction of medium-rise buildings in seismic regions: the XLAM case. *Structural Engineering International, 18,* 156–165.

European Committee for Standardization. (2004). *Eurocode 5: Design of timber structures.* Part 1-1: General – Common rules and rules for buildings. EN 1995-1-1. Brussels: CEN.

Fellmoser, P. and Blass, H. J. (2004) Influence of rolling shear modulus on strength and stiffness of structural bonded timber elements. CIB-W18/37-6-5, Edinburgh, U.K.

Forest Products Laboratory (FPL). (2010). *Wood handbook - wood as an engineering material* (centennial edition). Madison, WI, USA.

Guss, L. M. (1995). Engineered wood products: The future is bright. *Forest Products Journal, 45(7)*, 17.

Li, M., Lam, F. and Li, Y. (2014). Evaluating rolling shear strength properties of cross laminated timber by torsional shear tests and bending tests. In: Proceedings of the World Conference on Timber Engineering, WCTE 2004, Quebec City, Canada.

Li, Y. (2015). *Duration-of-load and size effects on the rolling shear strength of cross laminated timber* (Doctoral dissertation). The University of British Columbia, Canada.

McKeever, David B. (1997). *Pacific Rim Wood Market Report*. Forest Products Laboratory, Madison, Wisconsin, USA.

Mestek P., Kreuzinger, H. and Winter S. (2008). Design of cross laminated timber. In: Proceedings of the World Conference on Timber Engineering, WCTE 2008, Miyazaki, Japan.

Schaaf, A. (2010) *Experimental investigation of strength and stiffness properties for cross laminated timber* (Doctoral dissertation). Karlsruhe Institute of Technology, Germany

Stalnaker, Judith J., and Ernest C. Harris. (1989) *Structural Design in Wood.* New York: Springer.

Structurelam. (2014). *Cross laminated timber design guide.* BC: Structurelam.

Swanson Analysis System (SAS), Inc. (2011) *Ansys v 14.0*. Swanson Analysis System Inc., Houston, PA, USA

Western wood species book: Dimension lumber. (Vol. 1). (1979). Portland, Oregon: Western Wood Products Association.

Williamson, T. (2002). *APA engineered wood handbook.* New York: McGraw-Hill.

Yates, M., Linegar,M., and Dujic,B. (2008). Design of an 8-storey residential tower from cross laminated solid timber panels. In: Proceedings of the 19th International Scientific Conference on Wood is Good - Properties, Technology, Valorisation, Application. Zagreb, Croatia.

Yawalata D., Lam F. (2011). Development of technology for cross laminated timber building systems. Research report submitted to Forestry Innovation Investment Ltd., University of British Columbia, Vancouver, British Columbia, Canada

Zhou, Q. (2010). *Development of evaluation methodology for rolling shear properties in cross laminated timber* (Master Thesis). Chinese Academy of Forestry.

Zhou, Q., Gong, M., Chui, Y., and Mohammad, M. (2014). Measurement of rolling shear modulus and strength of cross laminated timber fabricated with black spruce. *Construction and Building Materials, 64,* 379-386.

Appendix

Appendix A. Dimensions for all testing specimens with 0.1 MPa manufacturing clamping pressure

Project No.:	Team2013-S01			**Test Span:**		838.2mm (33in)
Material:	Hem-Fir 5 Layers CLT			**Specimen Length:**		914.4mm (36in)
Wood Species:	Hemlock-Fir			**Clamping Pressure(MPa):**		0.1 MPa
Test Machine:	MTS 810			**Test Condition :**		22.7 °C, 51.6 % RH
Load Method:	Center Point Loading			**Date:**		30-Sep-13
Specimen No.	**Width (mm)**			**Depth (mm)**	**Weight (g)**	**Moisture Content (%)**
HF5-0.1-(1)-01	51.11	51.50	51.31	136.83	3235.2	10.0
HF5-0.1-(1)-02	49.67	50.50	50.94	137.12	3218.2	8.3
HF5-0.1-(1)-03	51.32	51.28	51.48	136.81	3327.1	9.2
HF5-0.1-(1)-04	50.73	50.28	50.90	137.05	3255.8	10.0
HF5-0.1-(1)-05	50.82	50.87	51.16	137.03	3260.1	9.2
HF5-0.1-(1)-06	50.87	50.94	51.08	137.22	3156.4	8.2
HF5-0.1-(1)-07	51.07	51.01	51.05	136.89	3225.0	9.6
HF5-0.1-(1)-08	50.96	51.10	51.12	137.76	3216.9	10.0
HF5-0.1-(1)-09	50.85	50.82	51.07	137.75	3275.4	10.2
HF5-0.1-(1)-10	50.67	50.80	51.97	137.44	3330.7	9.5
HF5-0.1-(1)-11	50.55	50.75	50.65	137.07	3262.7	9.3
HF5-0.1-(1)-12	50.92	49.94	50.76	138.02	3165.7	8.8
HF5-0.1-(1)-13	50.93	51.35	50.53	137.30	3263.2	9.5
HF5-0.1-(1)-14	51.47	51.37	51.29	137.66	3312.8	9.7
HF5-0.1-(1)-15	51.09	50.61	50.24	137.39	3241.5	9.6
HF5-0.1-(1)-16	51.16	51.16	51.01	136.80	3299.3	11.0
HF5-0.1-(1)-17	50.87	50.21	50.79	137.08	3113.3	8.0
HF5-0.1-(1)-18	51.24	51.51	51.22	136.83	3337.3	9.3
HF5-0.1-(1)-19	51.03	50.51	51.20	137.07	3292.5	9.5

Specimen No.	Width (mm)			Depth (mm)	Weight (g)	Moisture Content (%)
HF5-0.1-(1)-20	50.71	51.26	50.98	137.04	3172.4	9.3
HF5-0.1-(1)-21	51.61	51.50	51.31	137.36	3261.7	8.5
HF5-0.1-(1)-22	50.62	50.60	51.27	137.31	3205.0	9.6
HF5-0.1-(1)-23	51.25	51.34	50.84	137.67	3233.2	9.7
HF5-0.1-(1)-24	51.76	51.05	50.43	137.85	3224.8	9.6
HF5-0.1-(1)-25	50.55	50.80	51.67	137.48	3278.4	10.3
HF5-0.1-(1)-26	50.91	51.15	51.25	137.13	3269.4	9.8
HF5-0.1-(1)-27	48.70	50.55	51.28	137.79	3146.1	8.2
HF5-0.1-(1)-28	50.85	50.83	51.65	137.24	3306.6	9.5
HF5-0.1-(1)-29	51.14	50.98	51.52	137.51	3326.5	9.5
HF5-0.1-(1)-30	52.07	52.17	50.22	137.67	3397.1	10.5
HF5-0.1-(1)-31	52.15	51.05	52.01	137.58	3377.9	13.2
HF5-0.1-(2)-01	51.06	51.44	51.18	136.74	3129.8	10.0
HF5-0.1-(2)-02	51.45	50.94	51.45	137.02	3227.3	10.4
HF5-0.1-(2)-03	50.46	51.16	50.72	137.03	3271.1	10.0
HF5-0.1-(2)-04	50.80	50.45	51.17	137.65	3208.1	7.9
HF5-0.1-(2)-05	51.01	50.94	50.39	136.71	3286.4	9.2
HF5-0.1-(2)-06	50.48	50.15	51.03	137.57	3327.8	8.7
HF5-0.1-(2)-07	51.31	51.36	51.47	137.19	3320.6	8.9
HF5-0.1-(2)-08	51.29	50.54	50.95	137.55	3300.9	9.8
HF5-0.1-(2)-09	50.63	51.43	50.77	137.19	3191.2	9.3
HF5-0.1-(2)-10	50.91	50.90	51.44	137.98	3192.2	8.5
HF5-0.1-(2)-11	50.94	50.80	50.85	137.56	3271.9	10.8
HF5-0.1-(2)-12	48.63	49.78	50.44	137.28	3211.7	9.1
HF5-0.1-(2)-13	50.41	51.51	51.50	137.51	3174.1	9.1
HF5-0.1-(2)-14	50.96	50.71	51.55	137.60	3162.7	8.2
HF5-0.1-(2)-15	51.11	50.22	51.50	137.28	3374.1	9.4
HF5-0.1-(2)-16	50.82	52.11	50.87	136.55	3162.2	10.0
HF5-0.1-(2)-17	50.12	49.33	51.19	137.00	3157.0	12.4

Specimen No.	Width (mm)			Depth (mm)	Weight (g)	Moisture Content (%)
HF5-0.1-(2)-18	50.53	51.14	50.34	137.08	3351.2	13.1
HF5-0.1-(2)-19	51.42	51.57	51.20	137.77	3267.8	8.5
HF5-0.1-(2)-20	51.13	50.43	50.03	136.37	3211.7	9.0
HF5-0.1-(2)-21	50.50	50.64	50.71	137.46	3332.2	9.3
HF5-0.1-(2)-22	50.58	50.77	50.98	137.33	3275.4	9.8
HF5-0.1-(2)-23	51.69	51.10	50.66	137.47	3436.5	10.2
HF5-0.1-(2)-24	51.05	50.82	51.36	137.15	3228.4	9.5
HF5-0.1-(2)-25	50.99	51.40	51.15	138.04	3272.7	9.2
HF5-0.1-(2)-26	51.35	51.00	51.02	137.60	3266.6	9.1
HF5-0.1-(2)-27	50.34	51.45	51.22	137.68	3247.0	9.8
HF5-0.1-(2)-28	50.61	50.44	50.66	137.75	3065.3	9.6
HF5-0.1-(2)-29	51.04	51.12	51.06	137.90	3128.4	9.3
HF5-0.1-(2)-30	50.86	50.97	50.99	137.40	3370.7	9.8
HF5-0.1-(2)-31	51.10	51.39	51.14	137.55	3366.6	10.4
HF5-0.1-(3)-01	50.05	50.19	51.87	137.10	3291.4	10.3
HF5-0.1-(3)-02	51.23	50.84	50.46	137.86	3235.2	8.5
HF5-0.1-(3)-03	51.48	51.10	50.75	137.41	3183.8	7.3
HF5-0.1-(3)-04	50.19	50.30	50.62	137.61	3130.8	9.3
HF5-0.1-(3)-05	50.99	51.25	51.04	137.26	3230.3	7.9
HF5-0.1-(3)-06	50.97	49.81	49.42	137.60	3330.9	9.2
HF5-0.1-(3)-07	50.82	50.48	49.73	137.37	3261.4	11.1
HF5-0.1-(3)-08	50.59	50.82	50.98	138.68	3055.6	9.1
HF5-0.1-(3)-09	51.23	51.46	50.47	137.65	3343.8	7.8
HF5-0.1-(3)-10	50.81	50.28	50.38	137.85	3315.9	9.1
HF5-0.1-(3)-11	50.89	50.66	50.95	137.38	3380.0	9.8
HF5-0.1-(3)-12	51.16	51.40	51.01	137.44	3346.3	9.5
HF5-0.1-(3)-13	51.13	50.37	50.92	137.42	3288.3	8.5
HF5-0.1-(3)-14	50.76	51.32	50.95	137.50	3156.9	8.9
HF5-0.1-(3)-15	50.97	51.32	51.34	137.40	3349.8	9.3

Specimen No.	Width (mm)			Depth (mm)	Weight (g)	Moisture Content (%)
HF5-0.1-(3)-16	51.12	50.48	50.44	137.67	3399.2	9.6
HF5-0.1-(3)-17	50.26	50.38	50.69	137.81	3183.6	8.5
HF5-0.1-(3)-18	51.32	51.40	51.82	137.72	3264.5	9.1
HF5-0.1-(3)-19	50.54	50.73	50.73	138.12	3193.2	9.5
HF5-0.1-(3)-20	50.95	51.02	51.31	137.53	3281.6	9.4
HF5-0.1-(3)-21	50.77	50.89	50.68	138.21	3260.3	12.2
HF5-0.1-(3)-22	51.34	51.36	51.67	137.79	3220.8	10.7
HF5-0.1-(3)-23	50.56	50.60	50.62	138.30	3312.5	11.4
HF5-0.1-(3)-24	51.52	51.25	51.38	138.08	3424.8	9.0
HF5-0.1-(3)-25	51.19	50.60	48.61	138.50	3302.4	7.9
HF5-0.1-(3)-26	51.13	50.36	51.52	137.63	3319.7	10.0
HF5-0.1-(3)-27	50.58	51.09	51.18	138.44	3300.5	9.2
HF5-0.1-(3)-28	51.07	51.00	50.96	138.17	3170.0	9.2
HF5-0.1-(3)-29	50.39	50.65	50.65	138.97	3175.7	9.8
HF5-0.1-(3)-30	51.14	50.82	51.24	137.86	3365.0	9.4
HF5-0.1-(3)-31	50.65	50.70	51.15	138.09	3334.4	9.4

Appendix B. Dimensions for all testing specimens with 0.4 MPa manufacturing clamping pressure

Project No.:	Team2013-S01			**Test Span:**		838.2mm (33in)
Material:	HemFir 5 Layers CLT			**Specimen Length:**		914.4mm (36in)
Wood Species:	Hemlock-Fir			**Clamping Pressure(MPa):**		0.4 MPa
Test Machine:	MTS 810			**Test Condition :**		22.7 °C, 51.6 % RH
Load Method:	Center Point Loading			**Date:**		30-Mar-14
Specimen No.	**Width (mm)**			**Depth (mm)**	**Weight (g)**	**Moisture Content (%)**
HF5-0.4-(3)-01	50.51	50.56	51.26	136.93	3415.7	11.3
HF5-0.4-(3)-02	50.76	51.01	51.16	138.08	3237.1	9.0
HF5-0.4-(3)-03	50.82	51.03	51.01	138.07	3411.4	9.6
HF5-0.4-(3)-04	50.97	51.32	50.95	136.75	3328.5	8.8
HF5-0.4-(3)-05	50.41	50.74	50.67	136.81	3256.3	9.2
HF5-0.4-(3)-06	51.08	50.53	51.16	137.57	3146.1	10.5
HF5-0.4-(3)-07	50.96	50.84	50.63	137.12	3134.0	8.2
HF5-0.4-(3)-08	51.10	51.21	50.79	137.92	3333.6	8.6
HF5-0.4-(3)-09	50.75	50.64	50.64	137.39	3211.0	9.8
HF5-0.4-(3)-10	51.37	50.60	51.33	137.47	3106.3	8.9
HF5-0.4-(3)-11	51.14	50.56	51.03	137.70	3191.3	9.9
HF5-0.4-(3)-12	51.11	50.50	50.57	136.96	3376.9	9.5
HF5-0.4-(3)-13	51.26	50.91	50.95	137.24	3185.2	10.7
HF5-0.4-(3)-14	51.11	50.84	51.37	137.66	3431.0	8.9
HF5-0.4-(3)-15	50.66	51.25	51.43	137.73	3185.1	9.8
HF5-0.4-(3)-16	50.59	50.89	50.60	137.67	3085.3	10.2
HF5-0.4-(3)-17	51.30	50.78	50.99	137.19	3420.6	11.3
HF5-0.4-(3)-18	50.57	51.14	50.53	137.31	3148.1	10.8
HF5-0.4-(3)-19	50.63	50.74	50.91	137.56	3426.7	10.0
HF5-0.4-(3)-20	50.98	51.37	50.82	137.14	3333.9	9.1
HF5-0.4-(3)-21	51.25	51.38	50.96	137.06	3135.5	7.9
HF5-0.4-(3)-22	50.55	51.12	51.16	137.72	3110.1	10.3

Specimen No.	Width (mm)			Depth (mm)	Weight (g)	Moisture Content (%)
HF5-0.4-(3)-23	50.46	50.87	51.05	137.14	3187.6	11.1
HF5-0.4-(3)-24	50.47	50.69	51.11	137.36	3362.6	9.4
HF5-0.4-(3)-25	50.80	50.79	50.82	137.62	3443.6	7.9
HF5-0.4-(3)-26	50.81	50.82	50.88	137.20	3236.8	8.2
HF5-0.4-(3)-27	51.01	50.55	51.37	137.35	3168.4	7.6
HF5-0.4-(3)-28	51.36	50.61	51.33	137.84	3119.7	8.9
HF5-0.4-(3)-29	51.02	51.36	50.80	137.46	3327.7	8.9
HF5-0.4-(3)-30	50.99	50.43	51.36	137.84	3093.1	9.8
HF5-0.4-(3)-31	50.82	50.71	51.17	136.90	3139.9	10.0
HF5-0.4-(3)-32	51.38	50.77	50.83	137.82	3376.7	11.5
HF5-0.4-(3)-33	51.13	50.61	50.58	137.11	3288.3	8.2
HF5-0.4-(3)-34	50.84	51.39	50.87	137.99	3342.2	8.1
HF5-0.4-(3)-35	51.14	51.09	50.90	137.19	3303.7	9.3
HF5-0.4-(3)-36	51.23	50.61	50.66	137.26	3082.7	9.1
HF5-0.4-(3)-37	50.75	50.95	51.27	138.20	3183.1	8.4
HF5-0.4-(3)-38	51.27	51.21	51.30	137.69	3227.6	8.6
HF5-0.4-(3)-39	51.29	50.77	51.16	137.79	3359.4	9.5
HF5-0.4-(3)-40	50.47	51.23	50.88	136.88	3323.3	8.7
HF5-0.4-(3)-41	50.66	50.70	51.23	137.02	3284.5	8.1
HF5-0.4-(3)-42	51.39	51.31	50.62	137.38	3146.8	9.2
HF5-0.4-(3)-43	51.32	50.51	51.08	137.06	3078.5	11.0
HF5-0.4-(3)-44	51.22	50.44	51.45	137.18	3449.6	7.8
HF5-0.4-(3)-45	51.04	50.92	51.02	136.91	3432.8	8.7
HF5-0.4-(3)-46	50.63	50.79	51.22	137.92	3148.9	11.4
HF5-0.4-(3)-47	51.30	50.90	50.83	138.00	3412.7	9.2
HF5-0.4-(3)-48	50.74	51.06	50.81	136.75	3341.4	9.8
HF5-0.4-(3)-49	50.52	50.44	51.37	137.33	3241.5	10.0
HF5-0.4-(3)-50	51.13	51.27	51.12	136.80	3409.0	7.8
HF5-0.4-(3)-51	50.50	51.37	50.60	137.64	3354.5	9.3

Specimen No.	Width (mm)			Depth (mm)	Weight (g)	Moisture Content (%)
HF5-0.4-(3)-52	51.35	50.40	50.86	136.78	3454.1	8.1
HF5-0.4-(3)-53	51.20	50.51	51.20	138.01	3118.3	10.0
HF5-0.4-(3)-54	51.29	51.08	50.72	138.25	3158.8	8.7
HF5-0.4-(3)-55	50.60	50.55	50.65	137.43	3213.3	8.5
HF5-0.4-(3)-56	50.77	51.38	50.87	137.37	3351.1	7.8
HF5-0.4-(3)-57	50.50	50.83	51.44	138.13	3226.3	8.0
HF5-0.4-(3)-58	50.86	50.50	50.79	137.51	3086.5	11.5
HF5-0.4-(3)-59	50.95	51.01	50.72	138.03	3265.2	9.0
HF5-0.4-(3)-60	51.24	51.08	51.07	138.19	3093.4	8.4

Appendix C. Modulus of Elasticity of 93 specimens from 0.1 MPa manufacturing clamping pressure panels

Specimen No.	Apparent MOE (GPa)	Specimen No.	Apparent MOE (GPa)
HF5-0.1-(1)-1S	4.707	HF5-0.1-(2)-19M	4.531
HF5-0.1-(1)-2S	4.593	HF5-0.1-(2)-20M	4.596
HF5-0.1-(1)-3S	5.150	HF5-0.1-(2)-23M	4.785
HF5-0.1-(1)-4S	4.569	HF5-0.1-(2)-24M	4.229
HF5-0.1-(1)-8S	4.056	HF5-0.1-(2)-30M	5.452
HF5-0.1-(1)-9S	3.881	HF5-0.1-(3)-6M	5.214
HF5-0.1-(1)-12S	4.206	HF5-0.1-(3)-8M	4.321
HF5-0.1-(1)-15S	4.506	HF5-0.1-(3)-13M	4.855
HF5-0.1-(1)-18S	4.444	HF5-0.1-(3)-14M	4.712
HF5-0.1-(1)-20S	4.226	HF5-0.1-(3)-17M	4.560
HF5-0.1-(2)-5S	5.069	HF5-0.1-(3)-19M	4.392
HF5-0.1-(2)-6S	4.551	HF5-0.1-(3)-20M	5.583
HF5-0.1-(2)-13S	4.360	HF5-0.1-(3)-24M	5.359
HF5-0.1-(2)-16S	4.614	HF5-0.1-(3)-26M	5.014
HF5-0.1-(2)-17S	4.181	HF5-0.1-(1)-7L	4.806
HF5-0.1-(2)-22S	4.662	HF5-0.1-(1)-11L	4.358
HF5-0.1-(2)-25S	4.036	HF5-0.1-(1)-19L	4.184
HF5-0.1-(2)-27S	4.819	HF5-0.1-(1)-22L	4.360
HF5-0.1-(2)-31S	4.605	HF5-0.1-(1)-23L	4.043
HF5-0.1-(3)-2S	5.096	HF5-0.1-(1)-27L	3.818
HF5-0.1-(3)-3S	4.446	HF5-0.1-(1)-28L	4.472
HF5-0.1-(3)-5S	4.721	HF5-0.1-(1)-29L	4.349
HF5-0.1-(3)-10S	5.667	HF5-0.1-(1)-30L	4.005
HF5-0.1-(3)-11S	5.089	HF5-0.1-(1)-31L	4.599
HF5-0.1-(3)-12S	5.436	HF5-0.1-(2)-1L	4.523
HF5-0.1-(3)-22S	4.971	HF5-0.1-(2)-3L	4.840
HF5-0.1-(3)-23S	5.156	HF5-0.1-(2)-4L	4.879
HF5-0.1-(3)-28S	4.273	HF5-0.1-(2)-7L	4.760
HF5-0.1-(3)-29S	3.877	HF5-0.1-(2)-8L	4.537
HF5-0.1-(3)-30S	4.939	HF5-0.1-(2)-9L	4.658
HF5-0.1-(1)-5M	4.629	HF5-0.1-(2)-12L	4.942
HF5-0.1-(1)-6M	4.972	HF5-0.1-(2)-18L	4.742
HF5-0.1-(1)-10M	4.900	HF5-0.1-(2)-21L	4.321

Specimen No.	Apparent MOE (GPa)	Specimen No.	Apparent MOE (GPa)
HF5-0.1-(1)-13M	5.052	HF5-0.1-(2)-26L	5.184
HF5-0.1-(1)-14M	4.495	HF5-0.1-(2)-28L	4.719
HF5-0.1-(1)-16M	4.228	HF5-0.1-(2)-29L	4.645
HF5-0.1-(1)-17M	4.504	HF5-0.1-(3)-1L	5.718
HF5-0.1-(1)-21M	4.716	HF5-0.1-(3)-4L	4.486
HF5-0.1-(1)-24M	4.022	HF5-0.1-(3)-7L	5.329
HF5-0.1-(1)-25M	4.361	HF5-0.1-(3)-9L	5.391
HF5-0.1-(1)-26M	4.050	HF5-0.1-(3)-15L	5.290
HF5-0.1-(2)-2M	5.041	HF5-0.1-(3)-16L	5.425
HF5-0.1-(2)-10M	3.893	HF5-0.1-(3)-18L	4.769
HF5-0.1-(2)-11M	5.375	HF5-0.1-(3)-21L	4.837
HF5-0.1-(2)-14M	4.464	HF5-0.1-(3)-25L	4.252
HF5-0.1-(2)-15M	5.452	HF5-0.1-(3)-27L	5.086
		HF5-0.1-(3)-31L	4.569

Appendix D. Modulus of Elasticity of 60 specimens from 0.4 MPa manufacturing clamping pressure panels

Specimen No.	Apparent MOE (GPa)	Specimen No.	Apparent MOE (GPa)
HF5-0.4-(3)-1	3.864	HF5-0.4-(3)-31	4.704
HF5-0.4-(3)-2	3.963	HF5-0.4-(3)-32	4.707
HF5-0.4-(3)-3	3.964	HF5-0.4-(3)-33	4.727
HF5-0.4-(3)-4	4.041	HF5-0.4-(3)-34	4.735
HF5-0.4-(3)-5	4.220	HF5-0.4-(3)-35	4.771
HF5-0.4-(3)-6	4.248	HF5-0.4-(3)-36	4.788
HF5-0.4-(3)-7	4.263	HF5-0.4-(3)-37	4.810
HF5-0.4-(3)-8	4.283	HF5-0.4-(3)-38	4.826
HF5-0.4-(3)-9	4.322	HF5-0.4-(3)-39	4.847
HF5-0.4-(3)-10	4.385	HF5-0.4-(3)-40	4.853
HF5-0.4-(3)-11	4.389	HF5-0.4-(3)-41	4.858
HF5-0.4-(3)-12	4.405	HF5-0.4-(3)-42	4.869
HF5-0.4-(3)-13	4.440	HF5-0.4-(3)-43	4.877
HF5-0.4-(3)-14	4.444	HF5-0.4-(3)-44	4.878
HF5-0.4-(3)-15	4.461	HF5-0.4-(3)-45	4.901
HF5-0.4-(3)-16	4.464	HF5-0.4-(3)-46	4.974
HF5-0.4-(3)-17	4.537	HF5-0.4-(3)-47	4.981
HF5-0.4-(3)-18	4.543	HF5-0.4-(3)-48	5.002
HF5-0.4-(3)-19	4.603	HF5-0.4-(3)-49	5.034
HF5-0.4-(3)-20	4.617	HF5-0.4-(3)-50	5.061
HF5-0.4-(3)-21	4.622	HF5-0.4-(3)-51	5.165
HF5-0.4-(3)-22	4.645	HF5-0.4-(3)-52	5.204
HF5-0.4-(3)-23	4.657	HF5-0.4-(3)-53	5.205
HF5-0.4-(3)-24	4.662	HF5-0.4-(3)-54	5.305
HF5-0.4-(3)-25	4.674	HF5-0.4-(3)-55	5.341
HF5-0.4-(3)-26	4.676	HF5-0.4-(3)-56	5.385
HF5-0.4-(3)-27	4.679	HF5-0.4-(3)-57	5.478
HF5-0.4-(3)-28	4.688	HF5-0.4-(3)-58	5.660
HF5-0.4-(3)-29	4.699	HF5-0.4-(3)-59	5.876
HF5-0.4-(3)-30	4.702	HF5-0.4-(3)-60	6.691

Appendix E. Ultimate loads for slower loading rate specimens (rate of loading = 2 mm/min) as Group S and Group M

Specimen No.	Ultimate Load (kN)	Specimen No.	Ultimate Load (kN)
HF5-0.1-(3)-23S	13.615	HF5-0.1-(3)-08M	14.027
HF5-0.1-(3)-28S	15.078	HF5-0.1-(3)-26M	16.558
HF5-0.1-(2)-27S	15.393	HF5-0.1-(2)-30M	16.844
HF5-0.1-(1)-12S	15.666	HF5-0.1-(2)-23M	17.193
HF5-0.1-(2)-17S	15.690	HF5-0.1-(3)-17M	17.237
HF5-0.1-(2)-25S	15.910	HF5-0.1-(3)-06M	17.471
HF5-0.1-(3)-30S	16.117	HF5-0.1-(1)-14M	17.787
HF5-0.1-(2)-31S	16.122	HF5-0.1-(1)-05M	18.623
HF5-0.1-(2)-13S	16.223	HF5-0.1-(3)-20M	18.911
HF5-0.1-(3)-12S	16.313	HF5-0.1-(1)-16M	18.989
HF5-0.1-(3)-22S	16.749	HF5-0.1-(1)-21M	19.123
HF5-0.1-(2)-16S	17.565	HF5-0.1-(1)-06M	19.190
HF5-0.1-(3)-29S	17.829	HF5-0.1-(3)-24M	19.375
HF5-0.1-(3)-02S	17.839	HF5-0.1-(1)-25M	19.396
HF5-0.1-(1)-20S	18.096	HF5-0.1-(1)-10M	19.538
HF5-0.1-(3)-10S	18.101	HF5-0.1-(1)-24M	19.619
HF5-0.1-(3)-05S	18.145	HF5-0.1-(1)-26M	19.651
HF5-0.1-(1)-15S	18.217	HF5-0.1-(1)-17M	20.487
HF5-0.1-(2)-22S	19.062	HF5-0.1-(3)-14M	20.628
HF5-0.1-(1)-09S	19.166	HF5-0.1-(2)-14M	20.858
HF5-0.1-(2)-06S	19.641	HF5-0.1-(2)-15M	21.056
HF5-0.1-(1)-01S	19.752	HF5-0.1-(1)-13M	21.179
HF5-0.1-(1)-18S	19.767	HF5-0.1-(3)-13M	21.668
HF5-0.1-(1)-08S	19.909	HF5-0.1-(2)-10M	21.774
HF5-0.1-(1)-02S	20.286	HF5-0.1-(2)-11M	21.905
HF5-0.1-(3)-03S	21.443	HF5-0.1-(2)-02M	22.019
HF5-0.1-(1)-04S	21.697	HF5-0.1-(2)-20M	22.614
HF5-0.1-(2)-05S	21.771	HF5-0.1-(3)-19M	22.721
HF5-0.1-(3)-11S	21.870	HF5-0.1-(2)-19M	22.967
HF5-0.1-(1)-03S	22.387	HF5-0.1-(2)-24M	25.674

Appendix F. Ultimate loads for faster loading rate specimens (rate of loading = 20 mm/min) as Group L

Specimen No.	Ultimate Load (kN)
HF5-0.1-(3)-18L	14.738
HF5-0.1-(2)-04L	16.455
HF5-0.1-(1)-29L	17.738
HF5-0.1-(1)-23L	17.777
HF5-0.1-(3)-27L	17.919
HF5-0.1-(1)-27L	18.391
HF5-0.1-(2)-08L	18.948
HF5-0.1-(2)-28L	19.435
HF5-0.1-(1)-30L	19.465
HF5-0.1-(1)-28L	19.497
HF5-0.1-(3)-09L	19.511
HF5-0.1-(3)-25L	19.671
HF5-0.1-(2)-29L	19.703
HF5-0.1-(2)-09L	19.822
HF5-0.1-(3)-16L	19.845
HF5-0.1-(1)-22L	20.008
HF5-0.1-(2)-18L	20.243
HF5-0.1-(3)-21L	20.283
HF5-0.1-(2)-12L	20.455
HF5-0.1-(1)-19L	20.652
HF5-0.1-(2)-07L	20.710
HF5-0.1-(1)-11L	20.921
HF5-0.1-(2)-21L	20.921
HF5-0.1-(1)-07L	21.079
HF5-0.1-(2)-01L	21.339
HF5-0.1-(3)-15L	21.900
HF5-0.1-(3)-07L	22.535
HF5-0.1-(2)-03L	23.054
HF5-0.1-(3)-01L	23.093
HF5-0.1-(2)-26L	23.327

Appendix G. Ultimate loads for 60 specimens with manufacturing clamping pressure of 0.4 MPa

Specimen No.	Ultimate Load (kN)	Specimen No.	Ultimate Load (kN)
HF5-0.4-(3)-15	15.199	HF5-0.4-(3)-11	20.857
HF5-0.4-(3)-49	16.824	HF5-0.4-(3)-24	20.858
HF5-0.4-(3)-31	17.536	HF5-0.4-(3)-42	21.031
HF5-0.4-(3)-46	17.546	HF5-0.4-(3)-36	21.093
HF5-0.4-(3)-57	17.689	HF5-0.4-(3)-39	21.093
HF5-0.4-(3)-48	17.826	HF5-0.4-(3)-55	21.108
HF5-0.4-(3)-41	18.087	HF5-0.4-(3)-29	21.111
HF5-0.4-(3)-30	18.269	HF5-0.4-(3)-54	21.168
HF5-0.4-(3)-2	18.623	HF5-0.4-(3)-40	21.214
HF5-0.4-(3)-33	18.730	HF5-0.4-(3)-23	21.238
HF5-0.4-(3)-17	18.756	HF5-0.4-(3)-27	21.238
HF5-0.4-(3)-18	19.009	HF5-0.4-(3)-52	21.395
HF5-0.4-(3)-34	19.027	HF5-0.4-(3)-19	21.525
HF5-0.4-(3)-59	19.139	HF5-0.4-(3)-12	21.662
HF5-0.4-(3)-32	19.253	HF5-0.4-(3)-21	21.728
HF5-0.4-(3)-35	19.256	HF5-0.4-(3)-60	21.743
HF5-0.4-(3)-50	19.291	HF5-0.4-(3)-45	22.091
HF5-0.4-(3)-37	19.439	HF5-0.4-(3)-44	22.141
HF5-0.4-(3)-26	19.599	HF5-0.4-(3)-3	22.344
HF5-0.4-(3)-38	19.691	HF5-0.4-(3)-22	22.691
HF5-0.4-(3)-9	19.930	HF5-0.4-(3)-1	22.721
HF5-0.4-(3)-13	20.080	HF5-0.4-(3)-28	23.029
HF5-0.4-(3)-51	20.101	HF5-0.4-(3)-20	23.483
HF5-0.4-(3)-56	20.304	HF5-0.4-(3)-7	23.554
HF5-0.4-(3)-47	20.382	HF5-0.4-(3)-5	24.081
HF5-0.4-(3)-43	20.445	HF5-0.4-(3)-4	24.174
HF5-0.4-(3)-58	20.451	HF5-0.4-(3)-6	24.204
HF5-0.4-(3)-25	20.480	HF5-0.4-(3)-16	24.535
HF5-0.4-(3)-53	20.588	HF5-0.4-(3)-8	24.648
HF5-0.4-(3)-14	20.815	HF5-0.4-(3)-10	25.745

Appendix H. The initial failure modes of 65 specimens successfully captured with high speed camera filming

As the initial failure instant of each specimen is possible to occur on either side of the beam, while the high speed camera is only capable to capture a single side of the beam, there were only 65 video footages that captured the failure instants on tape. The initial failures were analyzed and categorized into three failure modes, namely rolling shear failure (RS), tension perpendicular to grain failure (TP), and marginal failure (MF). The last type of initial failure covered all the videos which were possible to be either RS or TP failure, yet not able to judge as the frame lapse between images was 0.5 microsecond.

Specimen No.	Loading Rate (mm/min)	Initial Failure Mode	Failure Crack/Annual Ring Orientation
HF5-0.1-(1)-21M	2	MF	Type B
HF5-0.1-(1)-24M	2	RS	Type B
HF5-0.1-(2)-10M	2	TP	Type B
HF5-0.1-(2)-14M	2	TP	Type B
HF5-0.1-(2)-15M	2	RS	Type A
HF5-0.1-(2)-20M	2	TP	Type B
HF5-0.1-(2)-30M	2	MF	Type C
HF5-0.1-(3)-13M	2	MF	Type A
HF5-0.1-(3)-17M	2	RS	Type A
HF5-0.1-(3)-26M	2	RS	Type B
HF5-0.4-(3)-01	2	MF	Type B
HF5-0.4-(3)-02	2	RS	Type B
HF5-0.4-(3)-03	2	RS	Type C
HF5-0.4-(3)-07	2	MF	Type C
HF5-0.4-(3)-11	2	TP	Type B
HF5-0.4-(3)-12	2	RS	Type A
HF5-0.4-(3)-13	2	RS	Type C

Specimen No.	Loading Rate (mm/min)	Initial Failure Mode	Failure Crack/Annual Ring Orientation
HF5-0.4-(3)-16	2	RS	Type B
HF5-0.4-(3)-17	2	TP	Type B
HF5-0.4-(3)-19	2	MF	Type B
HF5-0.4-(3)-20	2	RS	Type B
HF5-0.4-(3)-23	2	TP	Type B
HF5-0.4-(3)-25	2	MF	Type B
HF5-0.4-(3)-32	2	RS	Type C
HF5-0.4-(3)-33	2	MF	Type B
HF5-0.4-(3)-34	2	RS	Type C
HF5-0.4-(3)-35	2	RS	Type A
HF5-0.4-(3)-36	2	MF	Type C
HF5-0.4-(3)-37	2	TP	Type B
HF5-0.4-(3)-39	2	TP	Type B
HF5-0.4-(3)-40	2	MF	Type B
HF5-0.4-(3)-42	2	TP	Type B
HF5-0.4-(3)-43	2	TP	Type B
HF5-0.4-(3)-44	2	MF	Type C
HF5-0.4-(3)-46	2	RS	Type B
HF5-0.4-(3)-47	2	RS	Type B
HF5-0.4-(3)-50	2	MF	Type B
HF5-0.4-(3)-51	2	TP	Type B
HF5-0.4-(3)-52	2	TP	Type B
HF5-0.4-(3)-54	2	RS	Type B
HF5-0.4-(3)-55	2	TP	Type B
HF5-0.4-(3)-56	2	RS	Type B
HF5-0.4-(3)-57	2	MF	Type B
HF5-0.1-(1)-11L	20	TP	Type B
HF5-0.1-(1)-19L	20	RS	Type A
HF5-0.1-(1)-22L	20	TP	Type B
HF5-0.1-(1)-23L	20	MF	Type C
HF5-0.1-(1)-28L	20	TP	Type C
HF5-0.1-(1)-29L	20	TP	Type B
HF5-0.1-(1)-30L	20	TP	Type B
HF5-0.1-(2)-01L	20	RS	Type A
HF5-0.1-(2)-03L	20	TP	Type B
HF5-0.1-(2)-04L	20	TP	Type C

Specimen No.	Loading Rate (mm/min)	Initial Failure Mode	Failure Crack/Annual Ring Orientation
HF5-0.1-(2)-08L	20	MF	Type B
HF5-0.1-(2)-18L	20	RS	Type B
HF5-0.1-(3)-01L	20	MF	Type B
HF5-0.1-(3)-07L	20	RS	Type A
HF5-0.1-(3)-15L	20	TP	Type B
HF5-0.1-(3)-16L	20	TP	Type B
HF5-0.1-(3)-18L	20	RS	Type C
HF5-0.1-(3)-21L	20	RS	Type B
HF5-0.1-(3)-23L	20	TP	Type B
HF5-0.1-(3)-29L	20	RS	Type B
HF5-0.4-(3)-28	40	TP	Type B
HF5-0.4-(3)-30	40	TP	Type B